Initial-stage reaction of methane examined by optical measurements of weak flames in a micro flow reactor with a controlled temperature profile

Initial-stage reaction of methane examined by optical measurements of

weak flames in a micro flow reactor with a controlled temperature profile

Takahiro Onda[1], Hisashi Nakamura[1], Takuya Tezuka[1], Susumu Hasegawa[1], and Kaoru Maruta[1,2]

1: Institute of Fluid Science, Tohoku University,

2-1-1 Katahira, Aoba-ku, Sendai, Miyagi 980-8577, Japan

2: International Combustion and Energy Laboratory, Far Eastern Federal University, 8 Suhanova

St., Vladivostok, 690950, Russia

Abstract

To examine methane oxidation at intermediate temperatures (*ca.* 900‑1200 K), chemiluminescence observation and laser-induced fluorescence (LIF) measurements for CH_2O and OH were conducted for methane weak flames in a micro flow reactor with a controlled temperature profile (MFR) at atmospheric and elevated pressures. Locations of CH_2O-LIF, chemiluminescence, and OH-LIF in MFR were arranged from the low temperature side at 1.0 and 5.0 bar. Spatial separation of methane oxidation was successfully demonstrated. One-dimensional computations with five detailed kinetic mechanisms were conducted. Computational profiles of CH_2O molar concentration, heat release rate (HRR), and OH molar concentration normalized by their own peak values were compared with experimentally obtained intensity profiles of the CH_2O-LIF, chemiluminescence, and OH-LIF. Computational results obtained with AramcoMech 1.3 showed better agreements with experimentally obtained results among the mechanisms employed. However, the flame position computed with AramcoMech 1.3 showed a slightly higher temperature region than the experimental flame position, indicating underprediction of methane reactivity. Sensitivity analysis identified a set of dominant reactions for weak flame positions. Rate constants of the identified reactions were modified within uncertainty to reproduce experimentally obtained weak flame positions. The modified mechanism also well predicted ignition delay times and flame speeds, and significant improvement of prediction was identified particularly for ignition delay times of lowest temperature and pressure investigated. Reaction path analysis highlighted the importance of *intermidiate-temperature oxidation chemistry for methane* such as $CH_3 \rightarrow CH_3O_2 \rightarrow CH_3O \rightarrow CH_2O$ reactions at higher pressures. Two-stage oxidation of methane was observed by chemiluminescence observation and numerical simulations at higher pressures (6.0‑10.0 bar).

3

1. Introduction

The development of combustion devices with higher efficiency and clean exhaust gas emissions is necessary to achieve sustainable development goals. The use of natural gas as an energy source is increasing in various fields because of its smaller environmental impacts. Methane is the major component of natural gas. The development of accurate chemical kinetics for methane oxidation is fundamentally important for effective design of combustion devices. Therefore, fundamental combustion properties of methane such as laminar flame speeds [1–9] and ignition delay times [10–12] have been obtained and used for mechanism construction and validation.

However, performance of chemical reaction mechanisms of methane at intermediate temperatures (*ca*. 900–1200 K), which are typically lowest temperatures of ignition experiments with shock tubes and rapid compression machines for methane, requires improvements because of the lack of ignition data in such intermediate-temperature conditions. The lack of ignition data prevails because fundamental experiments to assess the low reactivity of methane are difficult to conduct under such temperature conditions. Therefore, this study examines methane oxidation at intermediate temperatures (900-1200 K), in particular related to reactions involving methyl-peroxy radicals (hereafter termed as *intermediate-temperature oxidation chemistry for methane* in this study). De Vries and Petersen [13] obtained ignition delay times of methane using a shock tube at around 1000 K and 25 atm. Their results showed that computational ignition delay times simulated using various kinetic mechanisms were much longer than the experimentally obtained results. Burke et al. [14] obtained ignition delay times of methane using a rapid compression machine at temperatures of 900–1670 K and pressures of 10–20 atm. They also conducted computations with a kinetic mechanism including reactions between methyl radicals and molecular oxygen, for which Zhu and Lin emphasized the importance of ignition at

4

intermediate temperatures [15]. Computations reported from an earlier study [14] showed quantitative agreement with measured ignition delay times at 20 atm, but showed longer ignition delay times at 10 atm. Given the relative dearth of reports in the relevant literature, further investigation of methane oxidation at intermediate-temperature conditions must be done to support the development of accurate methane reaction mechanisms.

Accordingly, this study uses a micro flow reactor with a controlled temperature profile (MFR) [16–27] to investigate fundamental ignition characteristics of methane further. Actually, the weak flame in MFR stabilized at low velocity conditions has been known to represent ignition-related properties of test fuels [28]. Moreover, MFR has been used to examine ignition-related properties of various fuels [16–27].

For instance, experiments using MFR for DME [17], *n*-heptane [18], and diesel surrogates [19] have indicated three reaction zones in the weak flame regime. Ordinary transient two-stage ignition of hydrocarbons was observed as steady multiple weak flames showing three-stage oxidation (cool flame, partial oxidation to CO, and complete oxidation to CO_2) in MFR. Strong correlation with weak flame positions and the research octane number (RON) have also been demonstrated from the appearance of multiple weak flames of primary reference fuels (PRFs) [20] and toluene reference fuels (TRFs) [21]. For fuels without two-stage oxidation at atmospheric pressures such as C1–C4 alkanes, fuel reactivities have been evaluated based on the stabilized position of the weak flame in MFR, as an index of ignitability, i.e., a weak flame of lower/higher reactivity fuel is stabilized at higher/lower temperature region in MFR [22]. Furthermore, MFR has been applied for various fuels such as syngas [23], alkenes [24], and ammonia [25, 26].

Recently, laser-induced fluorescence (LIF) for CH_2O and OH has been applied for methane weak flames in MFR at atmospheric pressure, revealing CH_2O formation at approximately 1000

5

K in the upstream region of the chemiluminescence from main oxidation around 1200 K [27].

Because the *intermediate-temperature oxidation chemistry for methane* is expected to strengthen at higher pressures [14, 15], this study uses observations of CH_2O-LIF, OH-LIF and chemiluminescence for methane weak flames at atmospheric and elevated pressures to elucidate details of the *intermediate-temperature oxidation chemistry for methane*. For this purpose, experimentally obtained intensity profiles of CH_2O-LIF, OH-LIF and chemiluminescence were compared with computed profiles with some representative existing kinetic mechanisms for methane. Comparisons are expected to facilitate validation of kinetic mechanisms and suggest avenues for further improvement of methane reaction kinetics.

2. Experimental method

2.1. Micro flow reactor with controlled temperature profile (MFR)

A schematic of the micro flow reactor with a controlled temperature profile (MFR) is presented in Fig. 1. A quartz tube with 2 mm inner diameter was used as a reactor channel. The quartz tube was heated using a H_2/air flat-flame burner to form a stationary temperature profile for 300–1300 K along the inner surface of the reactor in the flow direction, as portrayed in Figs. 1 and 2. Hereinafter, *wall temperature* denotes the temperature of the reactor channel's inner surface. The wall temperature was measured using a K-type thermocouple inserted from the downstream side of the reactor. A stoichiometric CH_4/air mixture was supplied to the reactor. High-purity methane (99.9%) and synthetic air (O_2 21%; N_2 79%) were used for this study. The flow rates of methane and air were controlled by mass flow controllers. The inlet mean flow velocity of 2 cm/s was chosen for the weak flame regime at atmospheric pressure. The mixture mass flow rate was kept constant at elevated pressures (e.g., 1 cm/s at 2.0 bar and 0.4 cm/s at 5.0 bar). For elevated pressure experiments, the reactor pressure was controlled using a back

6

pressure valve installed at the reactor exit. The pressure was varied in this study: 1.0–10.0 bar.

The experimentally obtained weak flame position was defined as the peak position of the observed luminosity profile of band-pass-filtered chemiluminescence (431.4 nm transparent wavelength; 6.4 nm full width at half maximum, FWHM).
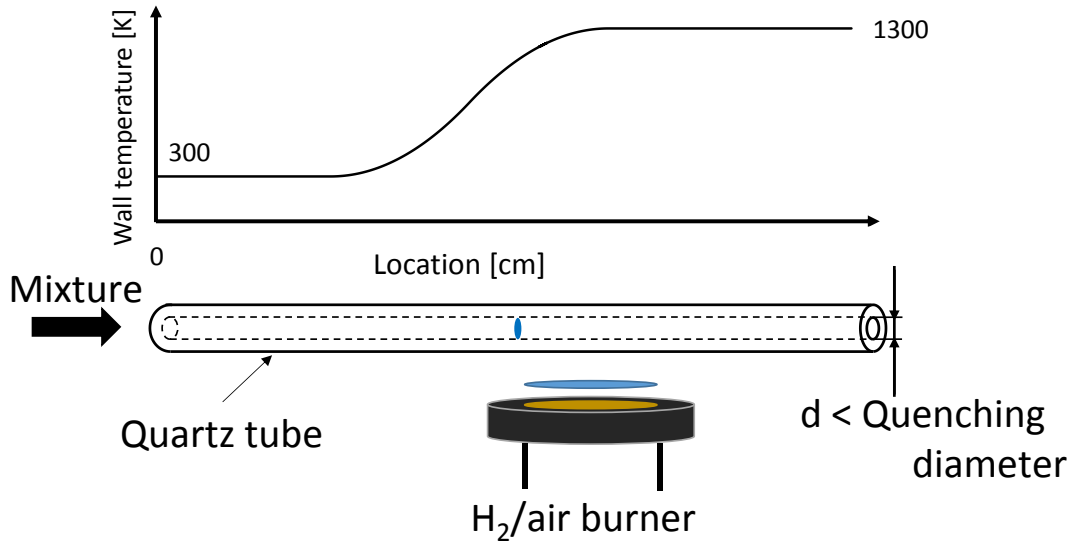
Fig. 1. Schematic of the micro flow reactor with a controlled temperature profile.
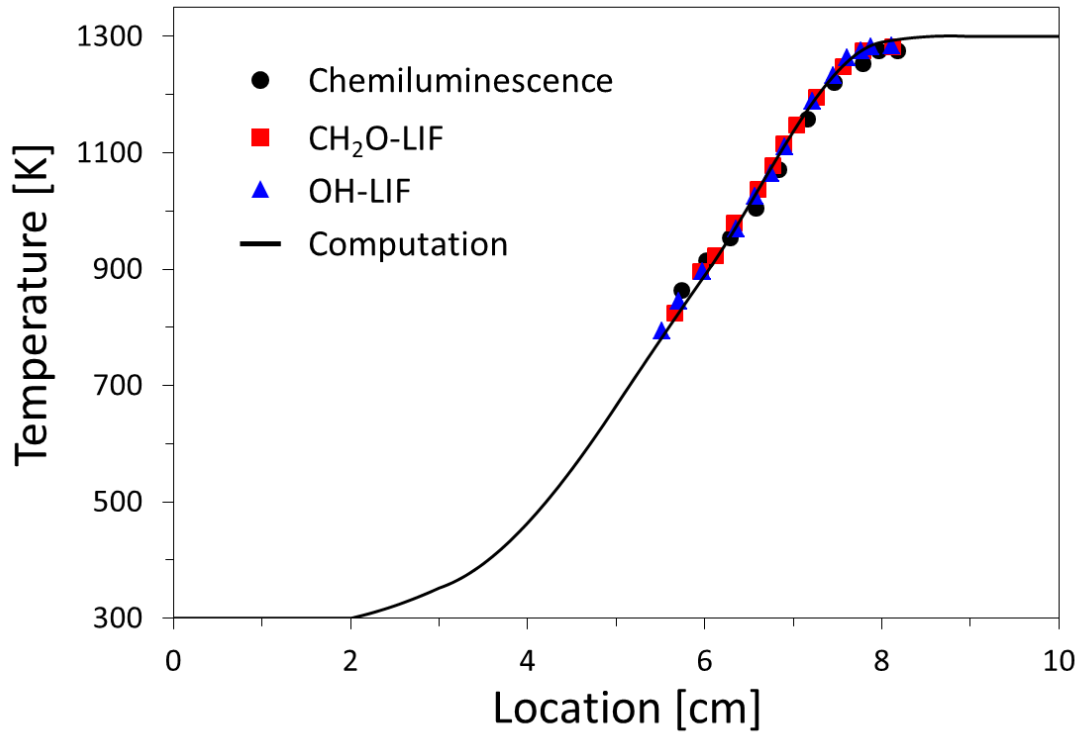
Fig. 2. Wall temperature profiles measured in experiments and used in computation.

2.2. Optical diagnostics

A schematic of the experimental setup for optical measurements is shown in Fig. 3. A pump laser, Nd:YAG laser (LOTIS TII, LS-2137/3), was used to obtain the second harmonic (523 nm) and the third harmonic (355 nm) laser light source. For OH-LIF, a dye laser (Fine Adjustment; Pulsare) containing a frequency control unit was used to obtain 283 nm. The $Q_1(7)$ line in the (1,0) band was used to detect OH excitation. A band-pass filter (313 nm transparent wavelength; 10 nm FWHM; and > 60% transmissivity) and two 300 nm high-pass filters were used to obtain clear signals without scattering of the dye laser light. Almost all relevant OH emissions were detected [29, 30]. Temperature dependence of the OH-LIF signal is negligibly small at the temperature conditions studied here [31]. Therefore, the OH-LIF image brightness was used without correction as the experimentally obtained OH-LIF intensity. The OH intensity profile

8

normalized by its peak value in the measurements was compared with the OH molar concentration profile normalized by its peak value in the computations. The peak value was taken at average values.

For CH₂O-LIF, the third harmonic from the Nd:YAG laser was used directly to excite the transition of $\tilde{A}^1 A_2 - \tilde{X}^1 A_1$ [29, 32, 33]. A 385 nm high-pass filter was used to capture wide spectrum lines of CH₂O-LIF and to prevent laser light scattering. The temperature dependence of the CH₂O-LIF signal was considered using the following procedure. The CH₂O-LIF signal is described by the following equation [34].

$$F = C_{exp} B_{12} N_1^0 I_v f_1 \frac{A_{21}}{A_{21} + Q_{21}} \tag{1}$$

Therein, C_{exp} is an experimentally derived constant, B_{12} represents the Einstein coefficient of absorption, A_{21} stands for the Einstein coefficient of spontaneous emission, I_v denotes the laser spectral irradiance, N_1^0 expresses the total CH₂O number of density, Q_{21} signifies the quenching rate, and f_1 is the population fraction of the *grand state* for the particular excitation. Because $A_{21} \ll Q_{21}$ for CH₂O, Eq. 1 is simplified as presented below.

$$F = C_{exp} B_{12} N_1^0 I_v f_1 \frac{A_{21}}{Q_{21}} \tag{2}$$

Here, f_1 and Q_{21} are temperature-dependent. Because the temperature dependence of f_1 is much stronger than that of Q_{21}, only the temperature dependence of f_1 was considered in this study. Kyritsis et al. [34] gave f_1 as a function of temperature, as shown below.

$$f_1 = \left(1 - e^{-1680.5/T}\right) \frac{40.1969 e^{-740/T}}{(1 + 0.134/T + 0.037/T^2) T^{3/2}} \tag{3}$$

Therefore, the brightness of a CH₂O-LIF image divided by f_1 was used as the compensated experimentally obtained CH₂O-LIF intensity. The gas-phase temperature is close to the wall temperature, even in the reaction zone in the weak flame regime [35]. Therefore, the wall temperature profile used for computations was employed to obtain the f_1 profile. The measured

CH$_2$O-LIF intensity normalized by its peak value was compared with the computational CH$_2$O molar concentration normalized by its peak value. The peak value was taken at average values.

An image-intensified charge-coupled device (ICCD) camera (DH334T-18-E3; Andor Co., Ltd.) with an ultraviolet (UV) lens was used as an optical receiver. The ICCD camera resolution was 1024×1024. The laser beam passed through a 1-mm-diameter aperture after being concentrated using cylindrical convex ($f = 200$ mm) and concave ($f = -40$ mm) lenses. The laser beam was introduced to the MFR channel from the downstream side. The laser pulse energy was approximately 3 mJ/pulse for LIF measurements of both CH$_2$O and OH. The YAG laser and ICCD were synchronized using a delay generator (DG645; Stanford Research Systems Inc.).

For observation of chemiluminescence from a weak flame, the ICCD camera with an optical band-pass filter (431.4 nm transparent wavelength, 6.4 nm FWHM) was used. The exposure time was set as 5 s. The chemiluminescence intensity profile was used directly for comparison without correction. The measured intensity profile of chemiluminescence normalized by its peak value was compared with the computational profiles of the heat release rate (HRR) normalized by its peak value. The peak value was taken at average values.

For all images obtained using LIF measurements and chemiluminescence observation, background subtraction image processing was conducted to obtain a better S/N ratio.
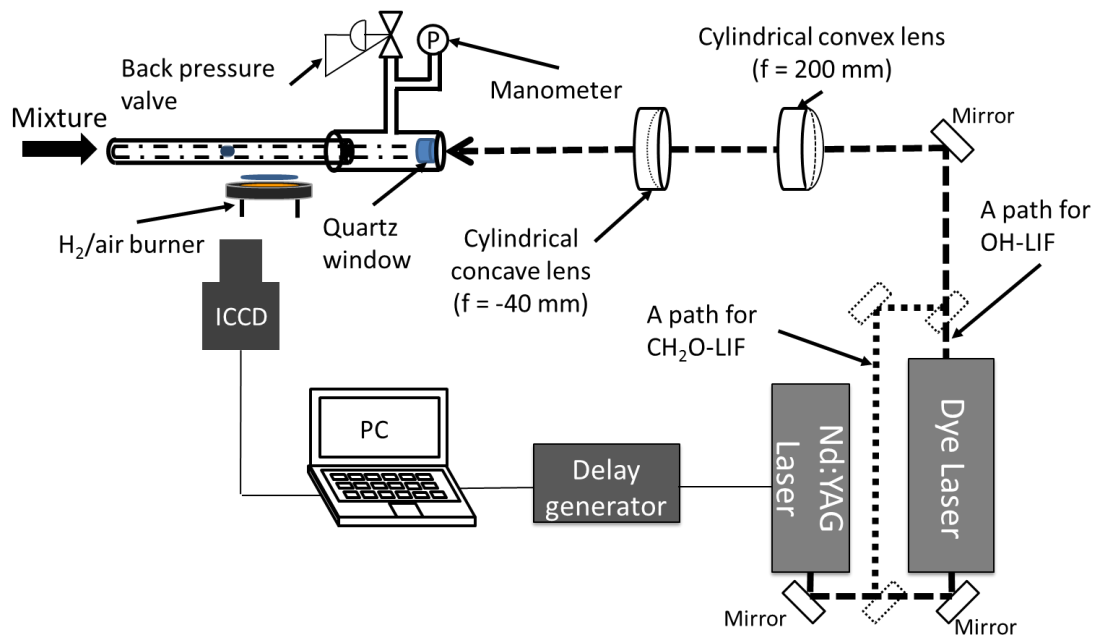
Fig. 3. Schematic of the experimental setup for optical measurements.

3. Computational methods

3.1. Simulation for micro flow reactor with a controlled temperature profile

Weak flames in the micro flow reactor can be modeled using a one-dimensional reactive

flow without a boundary layer [36]. This modeling can be realized using governing equations of

1-D planar flame together with additional heat transfer term between the gas and the reactor

wall to the gas-phase energy equation [36]. Therefore, modified PREMIX code with an

additional heat transfer term was used here as in earlier studies [16–27]. The wall temperature

profile (300–1300 K), which was the same as the measured profile, was used for computations,

as shown in Fig. 2. The computational domain was 10 cm long. As in experiments, a

stoichiometric methane/air mixture with constant mass flow rate (2 cm/s at 1.0 bar) was applied

at the inlet in computations. The computational weak flame position was defined as the peak

position of the HRR profile.

Five detailed reaction mechanisms were used for this study: GRI-Mech 3.0 (GRI 3.0) [37];

11

San Diego Mechanism (SD 2016) [38]; USC mech Version II (USC II) [39], AramcoMech 1.3 (Aramco 1.3) [40], and HP-mech 3.3 [41]. Computations with AramcoMech 2.0 and 3.0 were conducted but converged solutions were not obtained for the present micro flow reactor system. Therefore, the authors chose AramcoMech 1.3. To reduce computational cost, hydrocarbon species higher than C4 and related reactions were removed from Aramco 1.3.

3.2. Shock tube and RCM simulations

To validate details of reaction mechanisms modified in this study, computations of ignition delay times were conducted. Then computational ignition delay times were compared with experimental results obtained using a shock tube and a rapid compression machine (RCM) [14]. The AURORA package, ANSYS CHEMKIN-PRO v17.2 was used for computations of the ignition delay times. A constant-volume model was used for shock tube simulation. For RCM simulation, a variable-volume model was used to incorporate heat loss in RCM experiments. Volume–time histories calculated from non-reactive pressure traces were used as referred from an earlier report [14]. The ignition delay time was defined as the time from arrival of the shock wave at the endplate (for ST experiments) or the peak in pressure at the end of compression (in RCM experiments) to the maximum in dP/dt.

4. Results and discussion

4.1. Experimental results

Figure 4 presents images obtained from chemiluminescence observations and LIF measurements conducted at 1.0 and 5.0 bar. Luminous regions of the CH_2O-LIF image, the chemiluminescence image, and the OH-LIF image are located in this order from upstream in both pressure conditions. Results demonstrate the capability of LIF-measurements in weak flames studied in the micro flow reactor to elucidate spatially separated CH_2O formation in the

upstream region of the flame position and OH formation in the downstream region of the flame position during methane oxidation. Luminous regions of the CH_2O image, the chemiluminescence image, and the OH-LIF image at 5.0 bar shift to lower temperature sides than those at 1.0 bar, indicating that the methane reactivity at 5.0 bar is higher than that at 1.0 bar.
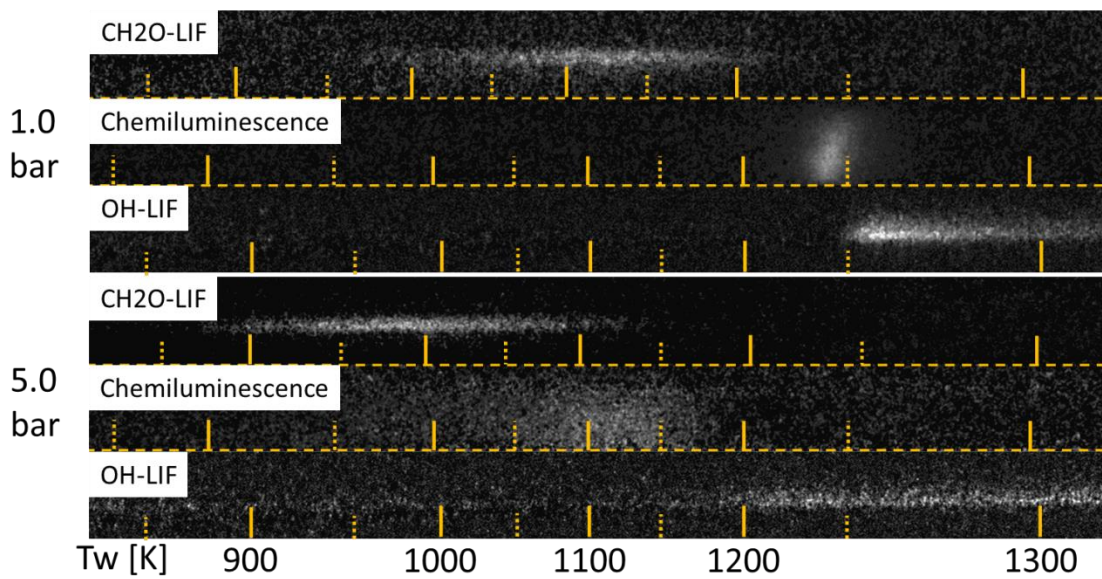

Fig. 4. Images obtained by chemiluminescence observation and LIF measurements at 1.0 and 5.0 bar.

4.2. Comparison with computational results

4.2.1. In the 1.0 bar condition

Figure 5 depicts the normalized chemiluminescence intensity and the normalized HRR at 1.0 bar. The HRR profile computed using GRI 3.0 shows a double peak, but those computed with the other mechanisms as well as the chemiluminescence profile respectively show single peaks. The peak position of the HRR profile computed with USC II shows better agreement with that of the chemiluminescence profile than those of the HRR profiles computed using other mechanisms.
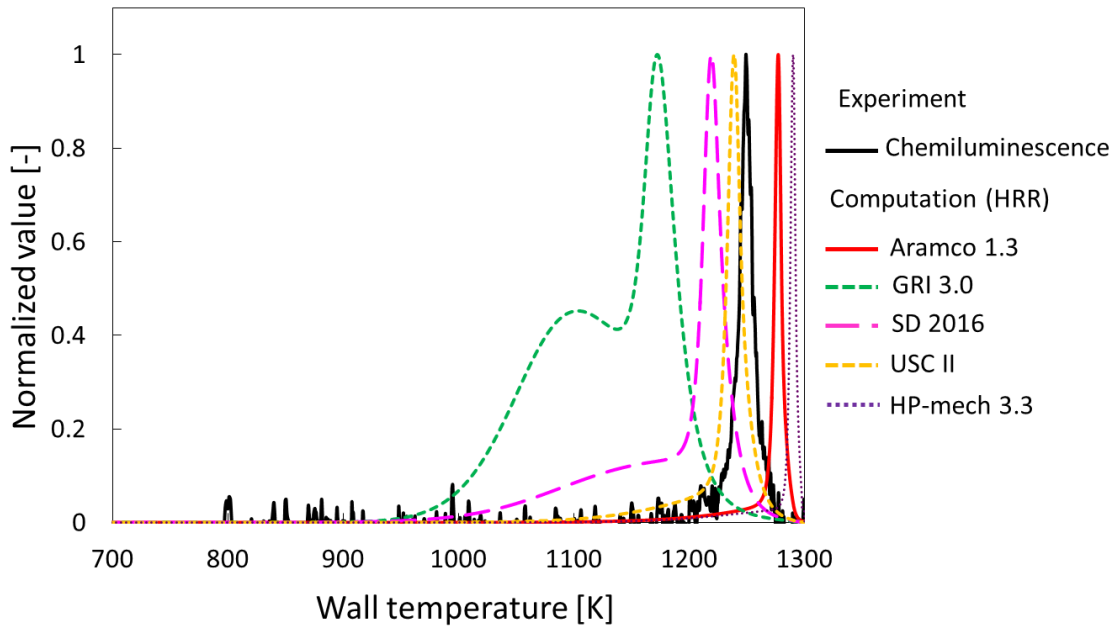
Fig. 5. Normalized chemiluminescence intensity and normalized HRR at 1.0 bar.

Figure 6 depicts the normalized CH_2O-LIF intensity and the normalized CH_2O molar concentration at 1.0 bar. All CH_2O profiles in both the experiment and computations show a single mild peak. The peak positions of the CH_2O profiles computed using USC II, Aramco 1.3 and HP-mech 3.3 exhibit better agreement with the experimentally obtained value compared to those computed using GRI 3.0 and SD 2016. The peak position of USC II and HP-mech 3.3 are placed at a lower and higher temperature region respectively than that of the experiment, whereas those of Aramco 1.3 is placed at higher temperature regions than that of the experiment. GRI 3.0 and SD2016 predict much lower temperatures of the peak positions than that in the experiment (over 100 K).
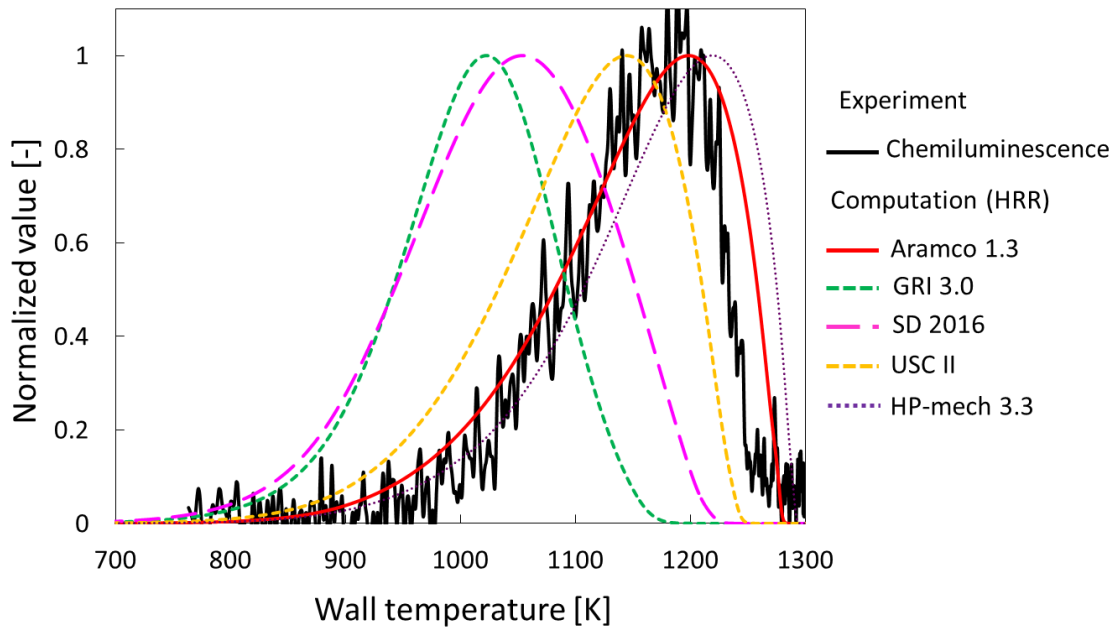
Fig. 6. Normalized CH_2O-LIF intensity and normalized CH_2O molar concentration at 1.0 bar.

Figure 7 depicts the normalized OH-LIF intensity and the normalized OH molar concentration at 1.0 bar. All OH profiles obtained from both experimental and computational procedures show a single sharp peak. The peak positions of the OH profiles computed using USC II and Aramco 1.3 display better agreement with that obtained using the experiment than those computed using GRI 3.0, SD 2016 and HP-mech. The peak position of USC II is placed at a lower temperature region than that indicated by the experiment, whereas those of Aramco 1.3 is placed at higher temperature regions than that of the experiment. These relations between the experimental result and model predictions for the peak positions of the OH profiles are similar to those for the CH_2O profiles.
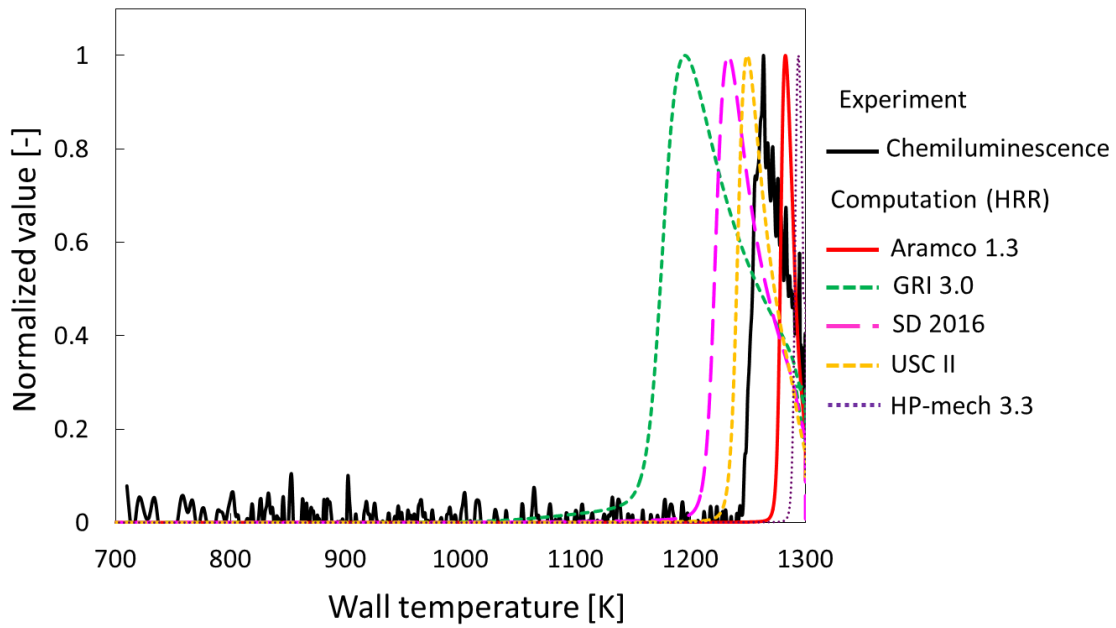
Fig. 7. Normalized OH-LIF intensity and normalized OH molar concentration at 1.0 bar.

4.2.2. In the 5.0 bar condition

Figure 8 depicts the normalized chemiluminescence intensity and the normalized HRR at

5.0 bar. The chemiluminescence profile seems to have a single peak in the high-temperature

region. It is known that HRR peaks around 800-1000 [K] and 1100 [K] are "partial oxidation up

to CO" and "complete oxidation. Furthermore, the former/latter are stronger/weaker when the

pressure is increased [42]. GRI 3.0, SD 2016, USC II and HP-mech 3.3 show a single peak in

each HRR profile. The temperatures at the peak positions of the HRR profiles with GRI 3.0, SD

2016 and USC II are approximately 200 K lower than that of the chemiluminescence profile.

The temperature at the peak positions of the HRR profiles with HP-mech 3.3 is approximately

100 K higher than that of the chemiluminescence profile. Aramco 1.3 shows double peaks in

their respective HRR profiles. Temperatures at the second peak positions of the HRR profiles

are slightly higher than that of the chemiluminescence profile (*ca.* 30 K). Aramco 1.3 shows that

the first peak of the HRR profile as much smaller than the second one. Among the five

16

mechanisms employed, the HRR profile computed using Aramco 1.3 shows better agreement
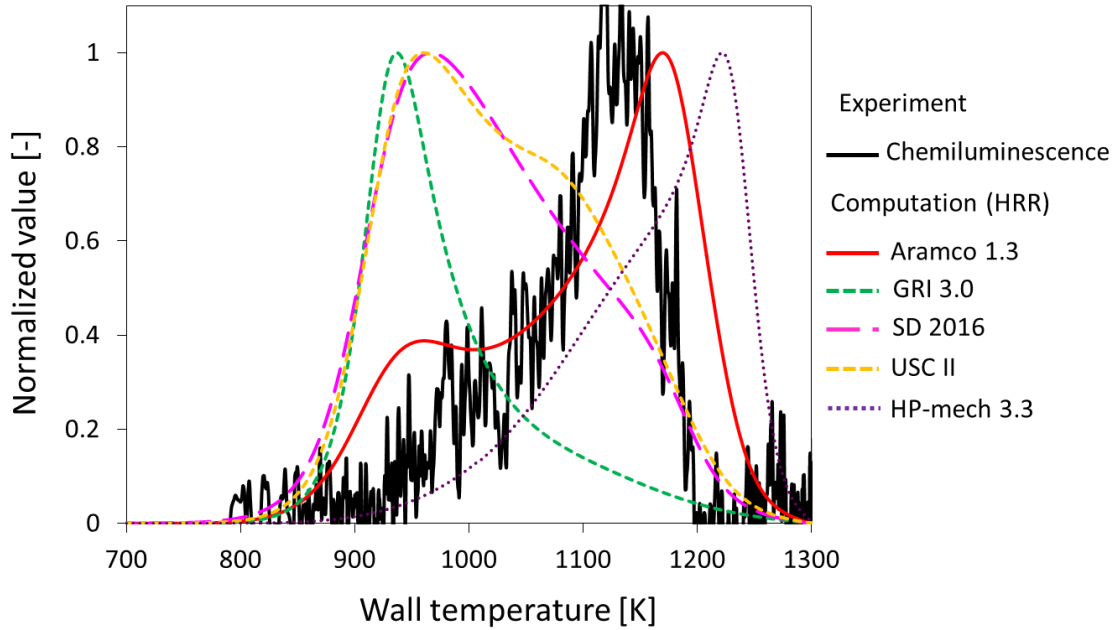
with the chemiluminescence profile.

Fig. 8. Normalized chemiluminescence intensity and normalized HRR at 5.0 bar.

Figure 9 depicts the normalized CH_2O-LIF intensity and the normalized CH_2O molar

concentration at 5.0 bar. All CH_2O profiles in the experiment and computations show a single

mild peak. The temperature at the peak position of the CH_2O profile in the experiment is

approximately 1000 K, whereas those in the computations are approximately 900 K, indicating

that Aramco 1.3, GRI 3.0, SD 2016 and USC II predicts the formation of CH_2O at lower

temperatures than those measured in experiment. The peak positions of the CH_2O profiles

computed using HP-mech 3.3 display better agreements with that obtained using the experiment

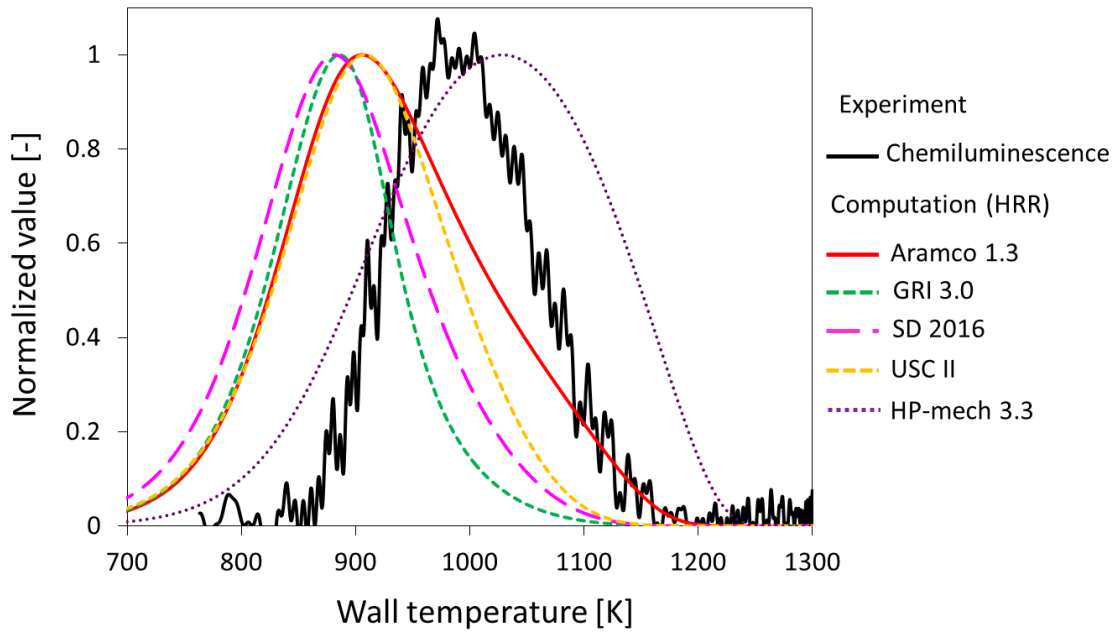than other four mechanisms employed in this study.

Fig. 9. Normalized CH_2O-LIF intensity and normalized CH_2O molar concentration at 5.0 bar.

Figure 10 depicts the normalized OH-LIF intensity and the normalized OH molar concentration at 5.0 bar. The OH-LIF intensity increases in the high-temperature region around 1200−1300 K. This tendency is also apparent in the OH profiles in the computations using all the mechanisms. However, quantitative comparison of the peak positions in the OH profiles at 5.0 bar is not reported here because the OH-LIF intensity profile is jagged as a result of a low S/N ratio at high pressure.
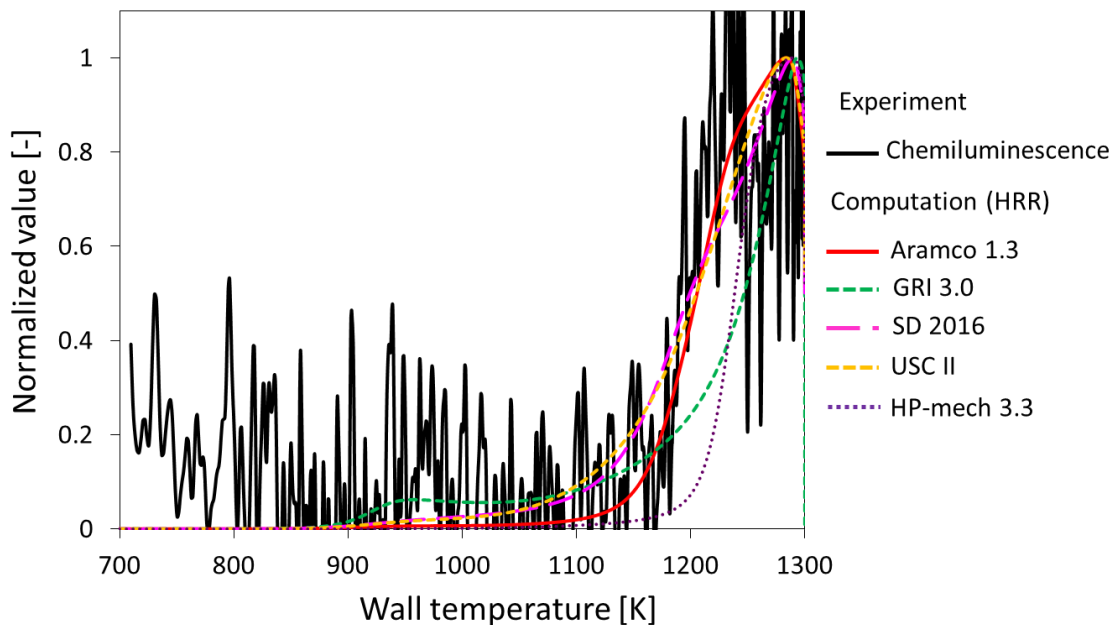
Fig. 10. Normalized OH-LIF intensity and normalized OH molar concentration at 5.0 bar.

4.2.3. Summary of comparison between experiments and computations

No mechanism used for this study was able to predict the experimentally obtained results perfectly. Computational results obtained using Aramco 1.3 and USC II showed better agreement with experimentally obtained results than that of GRI 3.0, SD 2016 and HP-mech 3.3 at 1.0 bar, whereas those obtained using Aramco 1.3 showed better agreement with experimentally obtained results than that with GRI 3.0, SD 2016 and HP-mech 3.3 at 5.0 bar. Therefore, modification of Aramco 1.3 can be proposed through detailed reaction analysis in this study. We also attempted modification of USC II. However, a key reaction pathway, *intermediate-temperature oxidation chemistry for methane*, which is discussed later, is not included in USC II. Therefore, modification of Aramco 1.3 showed better prediction for weak flames as they did for flame speeds and ignition delays. Accordingly, modification of Aramco 1.3 is discussed in the next section. For reference, explanation of the modification of USC II is attached in *Supplementary Materials*.

19

4.3. Modification of Aramco 1.3

4.3.1. Approach of the mechanism modification

Reactions that show high sensitivity for the weak flame position were chosen based on our sensitivity analysis. Sensitivity analysis for CH_2O mole concentration peak position was also conducted. However, as in the difficulty described in Section 4.4, mere weak flame position was used for the modification in present work. Rate parameters of the selected reactions were modified within the uncertainty of rate constants to reproduce better agreement with experimentally obtained results. Sensitivity coefficients for weak flame positions, S, are defined as the following equation [43].

$$S = \frac{2T_{2k} - 0.5T_{0.5k}}{1.5T_k} \qquad (6)$$

In that equation, T_{2k} and $T_{0.5k}$ respectively represent wall temperatures of the weak flame positions calculated using double-frequency and half-frequency factors of a reaction index k. T_k is that using an original frequency factor. Sensitivity coefficients for laminar flame speeds were obtained using first-order A-factor sensitivity analysis in flame speed calculation of PREMIX. From reactions with high-sensitivity coefficients for weak flame positions, hydrogen–oxygen reactions and reactions with high sensitivity coefficients for laminar flame speeds were excluded because the target of this study is the *intermediate-temperature oxidation chemistry for methane*. Rate constants of the selected reactions were surveyed from reports of the relevant literature. Arrhenius parameters were adjusted within the range of uncertainty of rate constants to reproduce better predictions for the peak positions of the experimentally obtained chemiluminescence, CH_2O-LIF, and OH-LIF profiles. After modification, the laminar flame speeds and ignition delay times were calculated using the modified mechanism. Comparisons with data in the literature were made to confirm how the modifications affected them.

4.3.2. Sensitivity analyses for weak flame position and laminar flame speed

Figure 11 presents results of sensitivity analyses for weak flame positions at 1.0 and 5.0 bar: the top 10 reactions at the respective pressure conditions. As the figure shows, reactions related with CH_3 radicals are sensitive to the weak flame positions. Figure 12 presents results of sensitivity analyses for laminar flame speeds at 300 K inlet temperature, atmospheric pressure, and equivalence ratios of 0.7, 1.0, and 1.3. As the figure shows, laminar flame speeds are sensitive to reactions related to H atom and HCO radical formation and consumption. From the reactions presented in Fig. 11, hydrogen–oxygen reactions (R17, R12, and R1) and reactions with high sensitivity coefficients for laminar flame speeds (R31, R27, and R30) were excluded. Nine reactions (R145, R189, R129, R128, R72, R76, R131, R148, and R144) were selected as candidate reactions for the present modification.
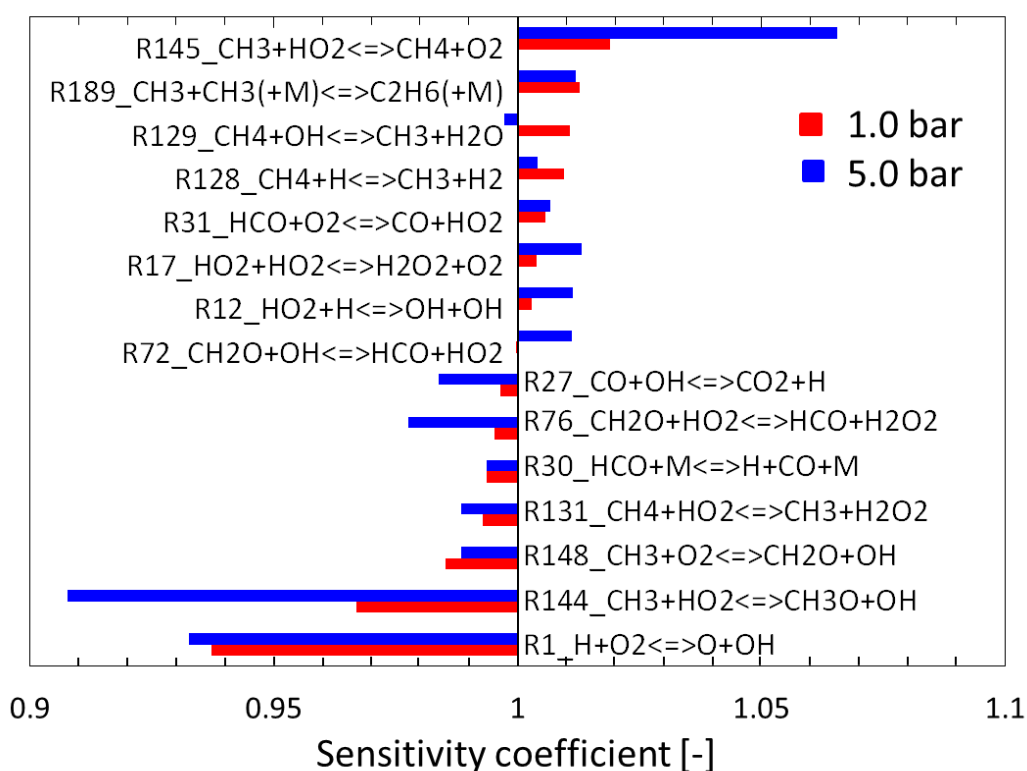
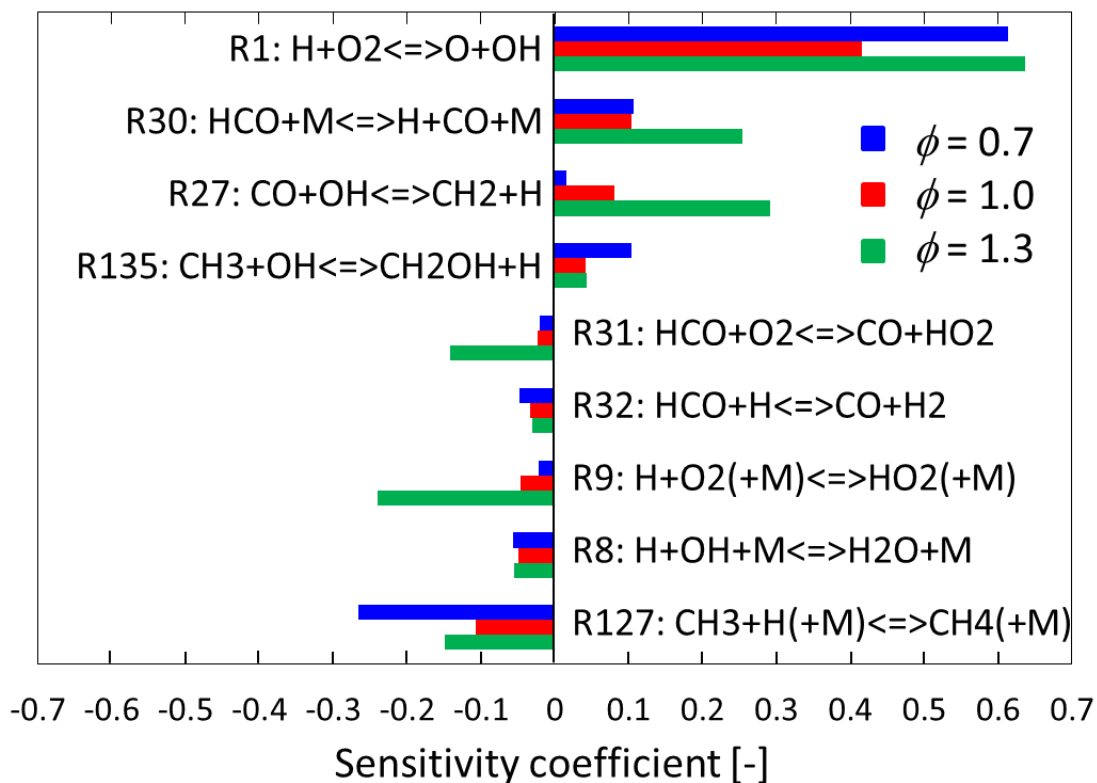Fig. 11. Sensitivity coefficients for weak flame positions at 1.0 and 5.0 bar.

Fig. 12. Sensitivity coefficients for laminar flame speeds at equivalence ratios of 0.7, 1.0, and 1.3.

4.3.3. R145: $CH_3 + HO_2 \iff CH_4 + O_2$

Figure 13 shows rate constants surveyed for R145. Symbols, lines with symbols, and solid lines respectively represent measured rate constants, estimated ones, and those used in the kinetic mechanisms. Rate constants of R145 were obtained experimentally by Hong et al. [44] and by Scire et al. [45], and theoretically by Mai et al. (canonical transition state theory: CVTST) [46], Jasper et al. (variable reaction coordinate TST: VRC-TST) [47], and Zhu and Lin (variational Rice–Ramsperger–Kassel–Marcus: variational RRKM) [15]. The experimental rate constants obtained by Hong et al. [44] and Scire et al. [45] show good mutual agreement, but large uncertainty (approximately a factor of 10) is apparent in the experimentally obtained

results. All rate constants obtained from theoretical studies show good agreement with the experimentally obtained rate constants within experimental uncertainty and within a factor of 5 from one another. Aramco 1.3 used the rate constant obtained by Jasper et al. [47], which is closer to the lower boundary of the experimental error bars. The present modification used a slightly higher rate constant than that used in Aramco 1.3 (within a factor of 2), as presented in Fig. 13, based on an experimental study reported by Hong et al. [44], to reproduce better predictions for peak positions of the experimentally obtained chemiluminescence, CH_2O-LIF and OH-LIF profiles.
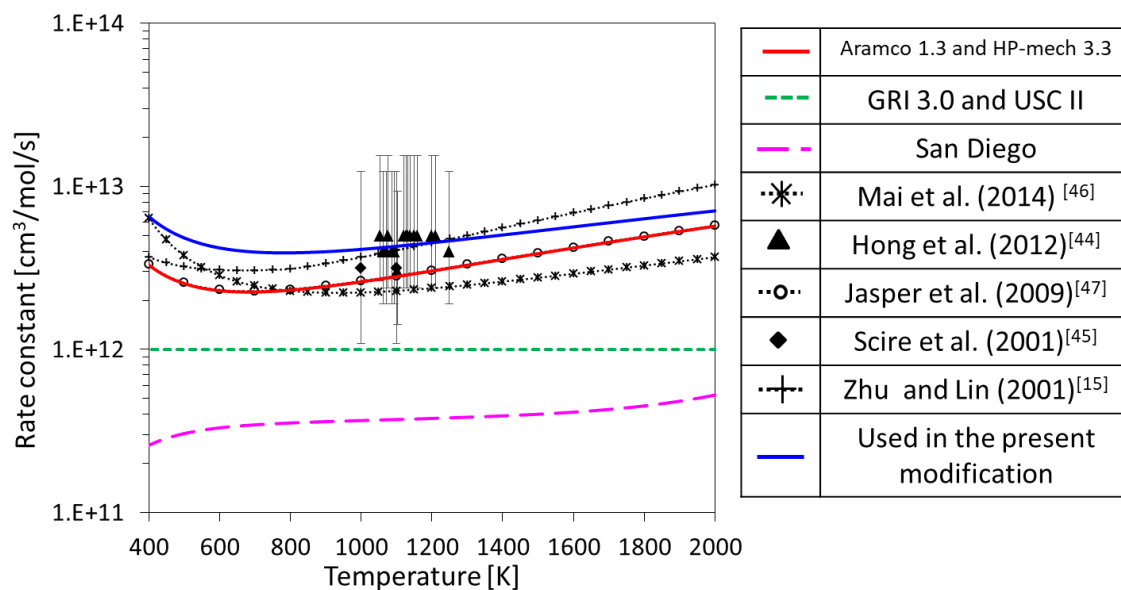
Fig. 13. Rate constants of R145: $CH_3 + HO_2 \iff CH_4 + O_2$.

4.3.4. R144: $CH_3 + HO_2 \iff CH_3O + OH$

Figure 14 presents rate constants surveyed for R144. Actually, R144 and R145 are reaction channels in the $CH_3 + HO_2$ reaction system. They are known to be important for predicting ignition delay times. Rate constants of R144 were obtained experimentally by Yan and

23

Krasnoperov [48], Hong et al. [44], and Scire et al. [45], and theoretically by Jasper et al. (VRC-TST) [47] and Zhu and Lin (microcanonical vibrational RRKM) [15]. The rate constant calculated by Zhu and Lin [15] is five times larger than that calculated by Jasper et al. [47]. Actually, Aramco 1.3 uses the constant calculated by Jasper et al. [47]. However, Jasper et al. reported that their theoretical calculations have uncertainty of 3 kcal/mol for the barrier height of 8.8 kcal/mol, which corresponds to factors of 5 and 2, respectively, for an uncertainty rate constants at 1000 and 2000 K. Faragó et al. [49] found new wells in the potential energy surface of the $CH_3 + HO_2$ reaction in their *ab initio* calculations. They also found a large discrepancy in the relative energy of the $CH_4 + {}^1O_2$ product channel between results reported by Jasper et al. (−25.56 kcal/mol) and by Zhu et al. (−29.4 kcal/mol). From these reasons, the uncertainty range of R144 is large. Here, the computational weak flame positions found using Aramco 1.3 were located at higher temperatures than the experimental weak flame positions at both pressure conditions. The sensitivity coefficient of R144 for the weak flame positions was much smaller than unity (strongly negative sensitivity to the weak flame position). These results indicate that the computational weak flame position will shift to lower temperatures with an increase in the rate constant of R144. Aramco 1.3 uses the rate constant reported by Jasper et al., but increased by a factor of 2, which is within its range of uncertainty. Compared to the rate constant originally calculated by Jasper et al., this modified rate constant exhibits better agreement with data obtained by Scrie et al. [45] and the most recent data reported by Yan and Krasnoperov [48].
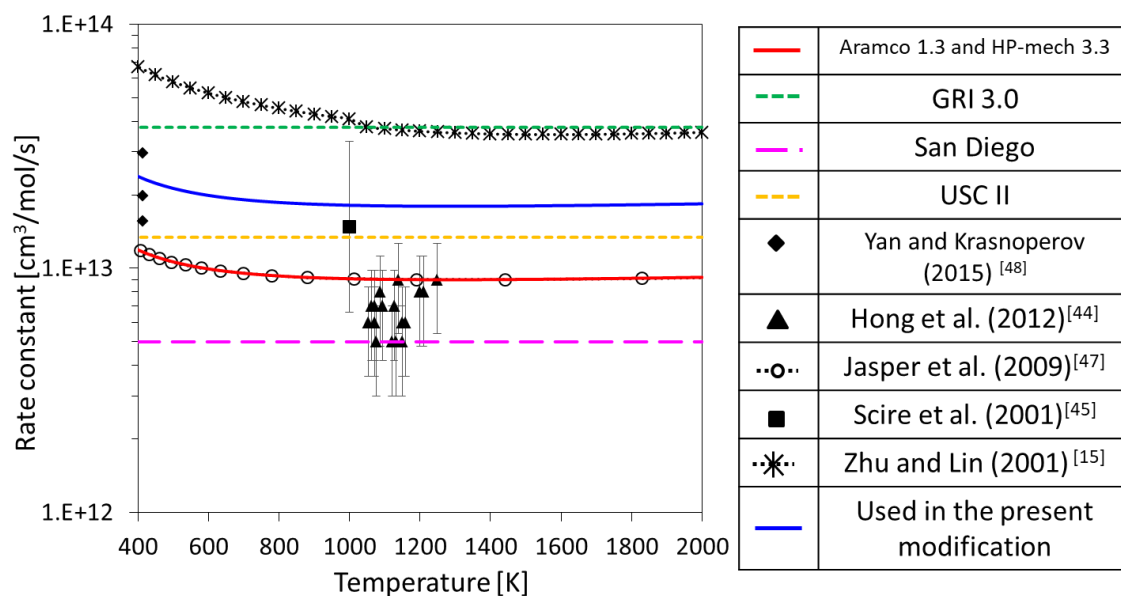
Fig. 14. Rate constant for R144: $CH_3 + HO_2 \Leftrightarrow CH_3O + OH$.

4.3.5. R189: $CH_3 + CH_3 (+M) \Leftrightarrow C_2H_6 (+M)$

Figure 15 presents rate constants surveyed for R189 of the high-pressure limit. Rate constants of

R189 of the high-pressure limit were obtained experimentally by Sangwan et al. [50], Wang et

al. [51], and Slagle et al. [52], and theoretically by Klippenstein et al. in 2006 (VRC-TST) [53]

and in 1999 (direct TST) [54], Wagner and Wardlaw (microcanonical variational RRKM) [55],

and Cobos and Troe (an analysis of the available experimental data using statistical adiabatic channel

theory) [56]. Aramco 1.3 uses the rate constant calculated by Wang et al. (2003). The present

study uses the rate constant calculated by Klippenstein et al. (2006) [53] because it shows good

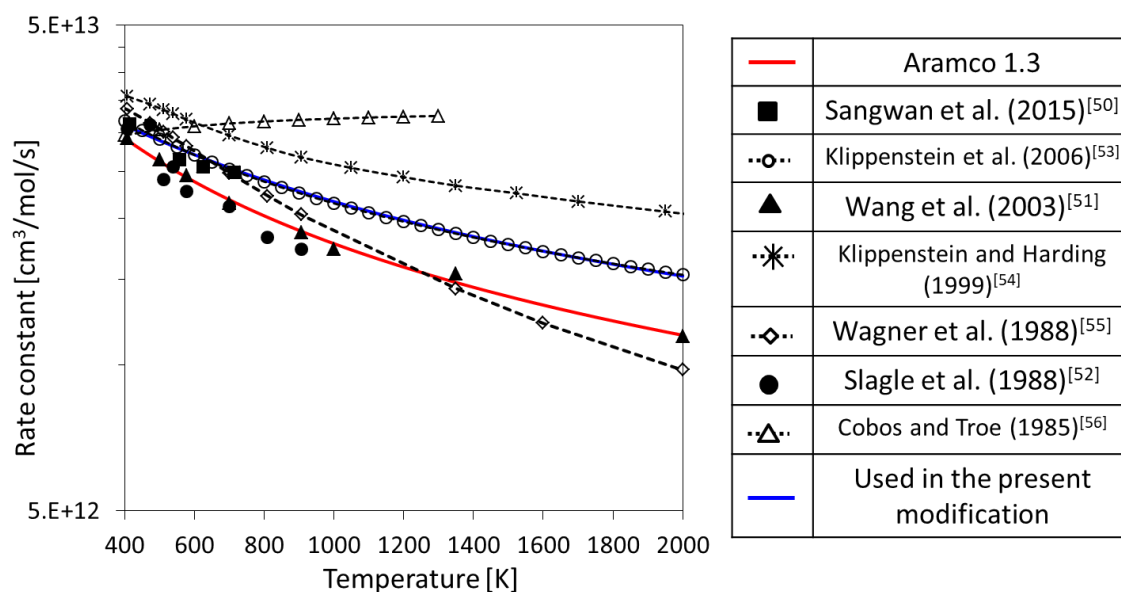agreement with the experimentally obtained rate constant reported recently by Sangwan et al.

[50].

25

Fig. 15. High-pressure limit rate constants for R189: $CH_3 + CH_3 (+M) \Longleftrightarrow C_2H_6 (+M)$.

Figure 16 presents the pressure dependence of the rate constants surveyed for R189. Rate constants of R189 near and below the high-pressure limit were measured by Hancock et al. [57], Du et al. [58], Slagle et al. [52], Hippler et al. [59], Macpherson et al. [60], and Glänzer et al. [61]. No theoretical rate constant for the low-pressure limit has been obtained. Two estimated values were proposed: the estimation by Wagner and Wardlaw [55], which is recommended by Baulch et al. [62]; and the estimation by Wang et al. [51], which was used in Aramco 1.3. However, the difference in rate constants between Aramco 1.3 and experiments becomes greater with increased temperature. Therefore, this study employs the high-pressure limit rate constant calculated by Klippenstein et al. (2006) [53], as described above, and that of the low-pressure limit estimated by Wagner and Wardlaw [55]. The TROE parameters were adjusted to reproduce experimentally obtained rate constants, as presented in Fig. 15.
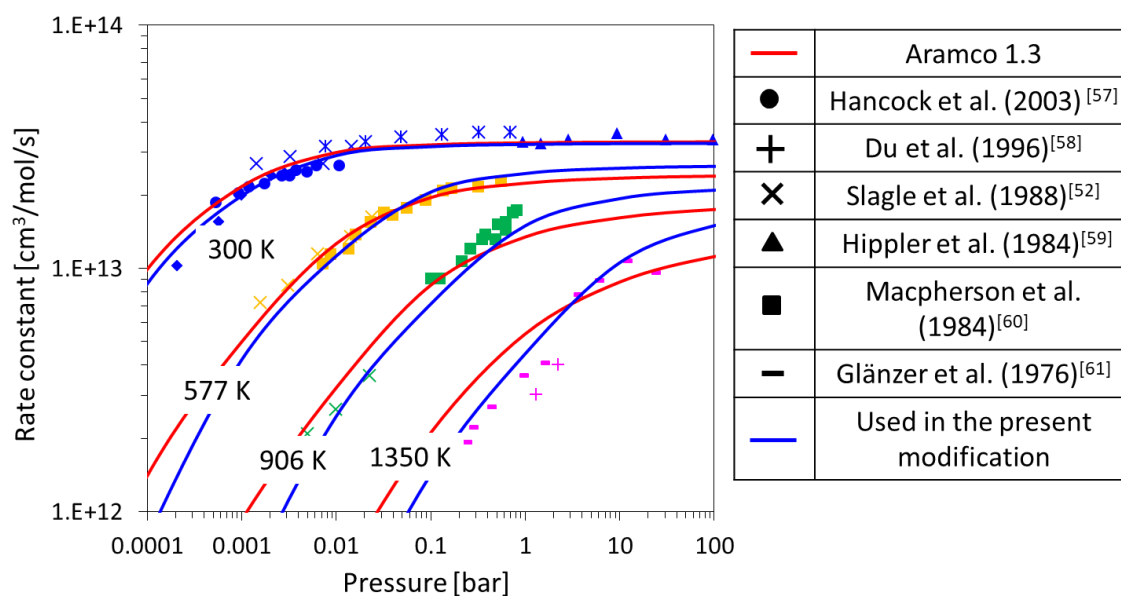
26

1.E+14

Rate constant [cm³/mol/s]

	Aramco 1.3
●	Hancock et al. (2003) [57]
+	Du et al. (1996)[58]
×	Slagle et al. (1988)[52]
▲	Hippler et al. (1984)[59]
■	Macpherson et al. (1984)[60]
—	Glänzer et al. (1976)[61]
	Used in the present modification

300 K

1.E+13

577 K

906 K   1350 K

1.E+12

0.0001   0.001   0.01   0.1   1   10   100

Pressure [bar]

Fig. 16. Pressure dependence of rate constants of R189: $CH_3 + CH_3$ (+M) <=> C_2H_6 (+M).

4.3.6. R129: $CH_4 + OH$ <=> $CH_3 + H_2O$

Rate constants for R129 were obtained experimentally by Hong et al. [44], Srinivasan et al. [63], Brykov et al. [64], Bonard et al. [65], Dunlop and Tully [66], and Madronich and Felder [67], and theoretically by Masgrau et al. (VTST including multidimensional tunneling calculations: VTST/MT) [68] and Schwartz et al. (TST) [69]. Experimental uncertainty was approximately a factor of 1.4 at around 1000 K. The rate constant used in Aramco 1.3 shows good agreement with experimentally obtained results within experimental uncertainty. Therefore, the rate constant of R129 was not modified in this study.

4.3.7. R128: $CH_4 + H$ <=> $CH_3 + H_2$

Rate constants of R128 were obtained experimentally by Sutherland et al. [70], Bryukov et al. [71], Baeck et al. [72], and Rabinowitz et al. [73], and theoretically by Kerkein and Clary (kinetic isotope effects: KIE from conventional TST) [74]. Experimental uncertainty was

27

approximately a factor of 1.5 around 1000 K. Rate constants used in Aramco 1.3 showed good

agreement with experimentally obtained results within experimental uncertainty. Therefore, the

rate constant of R128 was not modified in this study.

4.3.8. R72: $CH_2O + OH \iff HCO + HO_2$

Rate constants of R72 were obtained experimentally by Vasudevan et al. [75], Sivakumaran

et al. [76], Bott and Cohen [77], Zabarnick et al. [78], de Gurtechin et al. [79], Atkinson and

Pitts [80], Peeters and Mahnen [81], and Westenberg and Fristrom [82], and theoretically by Xu

et al. (VTST) [83] and Li et al. (CVTST with small–curvature tunneling correction method:

CVTST/SCT) [84]. Two theoretical rate constants showed a large difference (a factor of 10), but

the rate constant calculated by Xu et al. [83] showed good agreement with recent experimentally

obtained results reported by Vasudevan et al. [75] and Sivakumaran et al. [76]. The rate constant

used in Aramco 1.3 was almost equal to that computed by Xu et al. [83]. Therefore, the rate

constants of R72 were not modified in this study.

4.3.9. R76: $CH_2O + HO_2 \iff HCO + H_2O_2$

Rate constants of R76 were obtained experimentally by Eiteneer et al. [85], Hidaka et al.

[86], Jemi-Alade et al. [87], Hochgreb and Dryer [88], and Baldwin and Walker [89], and

theoretically by Li et al. (improved CVT: ICVT/SCT) [90]. Experimental uncertainty was

approximately a factor of 1.2 around 1100 K. The theoretical rate constant calculated by Li et al.

[90] showed good agreement with experimentally obtained results within the experimental

uncertainty. Aramco 1.3 uses the rate constant calculated by Li et al. [90]. Therefore, the rate

constant of R76 was not modified for this study.

4.3.10. R131: $CH_4 + HO_2 <=> CH_3 + H_2O_2$

Figure 17 presents rate constants surveyed for R131. Rate constants of R131 were obtained experimentally by Baldwin et al. [91] and theoretically by Carstensen et al. (TST) [92] and Aguilera-Iparraguirre et al. (TST) [93]. The rate constant calculated by Aguilera-Iparraguirre et al. [93] was a factor of 3 lower than that calculated by Carstensen et al. [92] at 1500 K. It agrees well with the experimentally obtained results reported by Baldwin et al. [91]. However, Aramco 1.3 uses a 1.5-times-higher rate constant than that calculated by Aguilera-Iparraguirre et al. [93]. The present modification employed the original rate constant calculated by Aguilera-Iparraguirre et al. [93].
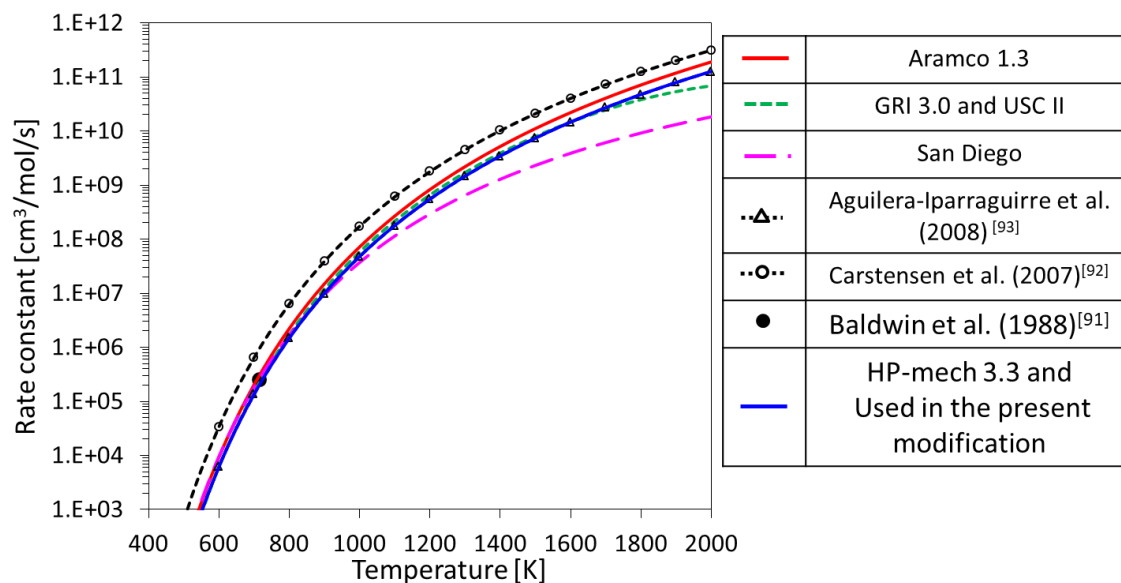
Fig. 17. Rate constants of R131: $CH_4 + HO_2 <=> CH_3 + H_2O_2$.

4.3.11. R148: $CH_3 + O_2 <=> CH_2O + OH$

Figure 18 presents rate constants surveyed for R148. Rate constants for R148 were obtained experimentally by Srinivasan et al. (2007) [94], (2005) [95], and Yu et al. [96], and theoretically

by Zhu et al. (RRKM) [97], Zellner and Ewig (RRKM) [98], and Reitel et al. (RRKM) [99]. All experimental rate constants were obtained at temperatures higher than 1400 K, with wide observed discrepancy among the data reported in the literature. The theoretical rate constants also show a large mutual discrepancy. R148 showed sensitivity coefficients for the weak flame positions lower than unity (negative sensitivity to the weak flame position); the HRR peaks were located at higher temperatures than the chemiluminescence peaks at 1.0 and 5.0 bar. Therefore, a higher rate constant than that used in Aramco 1.3 is necessary in the present temperature region of the micro flow reactor (below 1300 K) to reproduce the weak flame positions. Therefore, the rate constant of R148 was modified to a higher value than that used in Aramco 1.3 at low temperatures. It is similar to that used in Aramco 1.3 at high temperatures, as presented in Fig. 18. The rate constant used in the present modification at *intermediate temperatures* was set as closer to that obtained in the latest theoretical calculations by Srinivasan et al. (2007) [94] than that used in Aramco 1.3. Table 2 presents a list of modified reactions and their rate parameters used in the present study.
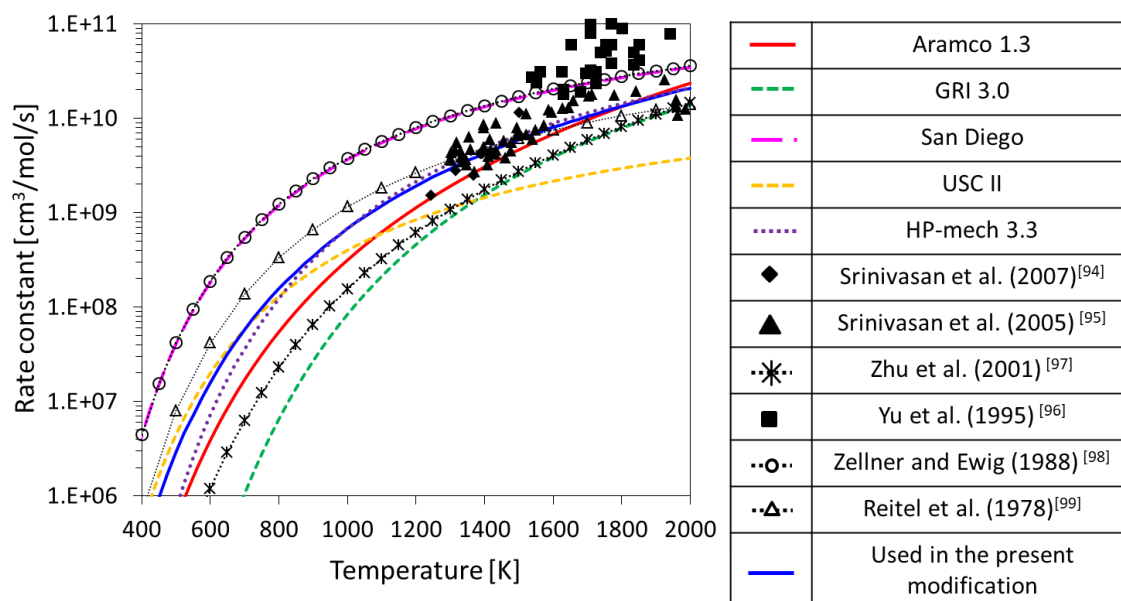

Fig. 18. Rate constant for R148: $CH_3 + O_2 \Longleftrightarrow CH_2O + OH$.

Table 2. Modified reactions and their rate parameters used in this study

		in cm3-mol-cal-sec units	
Reaction	A	n	E
R145_$CH_3+HO_2=CH_4+O_2$	4.0E+06	1.8	-2800
R144_$CH_3+HO_2=CH_3O+OH$	2.0E+12	0.269	-687.5
R189_$CH_3+CH_3(+M)=C_2H_6(+M)$	9.5E+14	-0.538	179
LOW	1.269E41	-7.0	2762
TROE 0.6	200	2000	1E+30
R131_$CH_4+HO_2=CH_3+H_2O_2$	1.13E+01	3.74	21010
R148_$CH_3+O_2=CH_2O+OH$	4.0E+04	2.0	8105

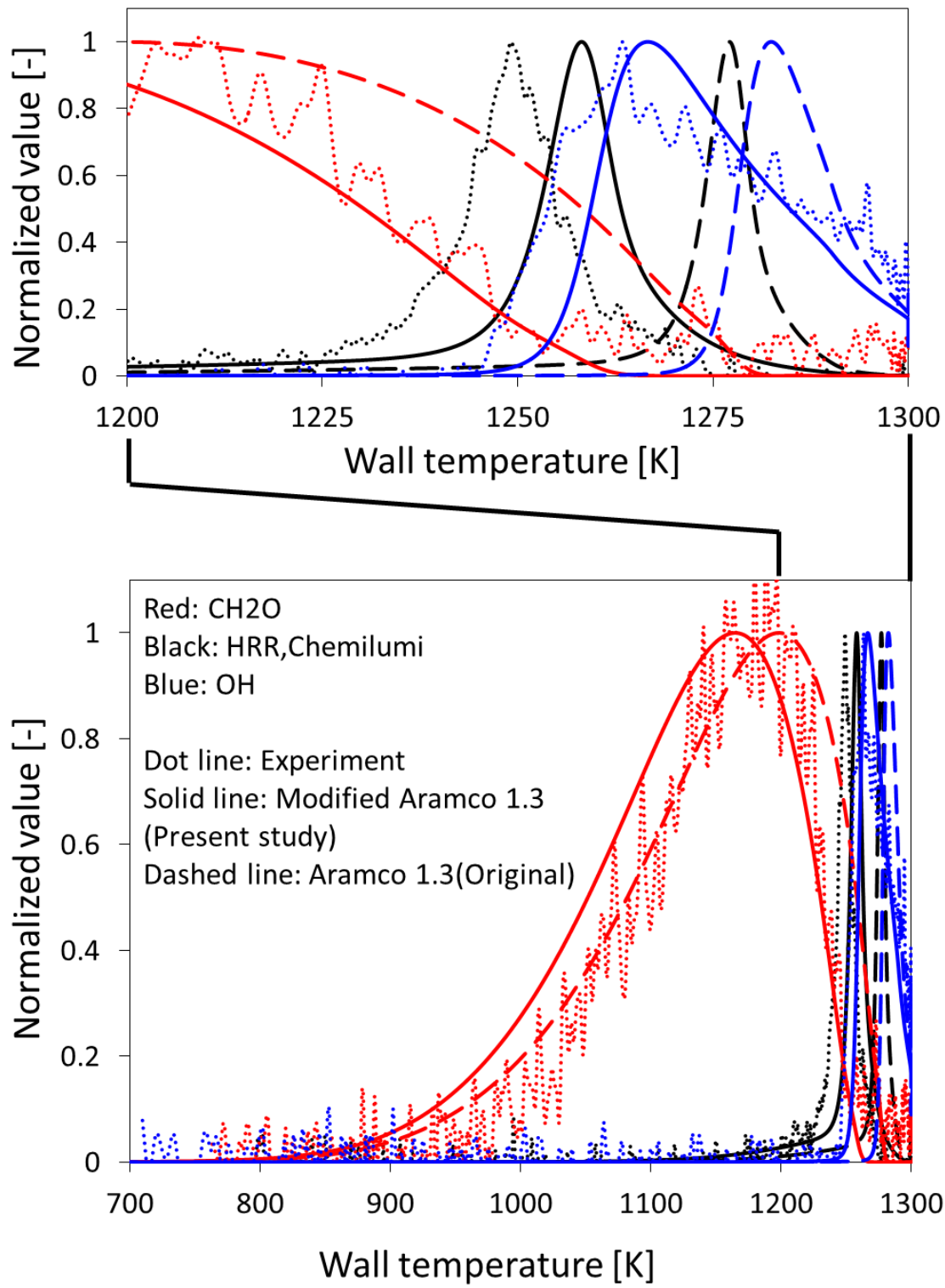4.3.12. Validation of the modified mechanism using experimentally obtained results for weak flames

Figure 19 depicts the normalized intensity of experimental images and the normalized HRR, CH_2O molar concentration, and OH molar concentration computed using the modified mechanism and Aramco 1.3 at 1.0 bar. The peak positions of the HRR, CH_2O, and OH profiles computed with the modified mechanism shift to the lower temperature region compared with those computed using Aramco 1.3, and are in better agreement with those obtained by experiments than those computed using Aramco 1.3. The present modification improved predictions of experimental weak flames.
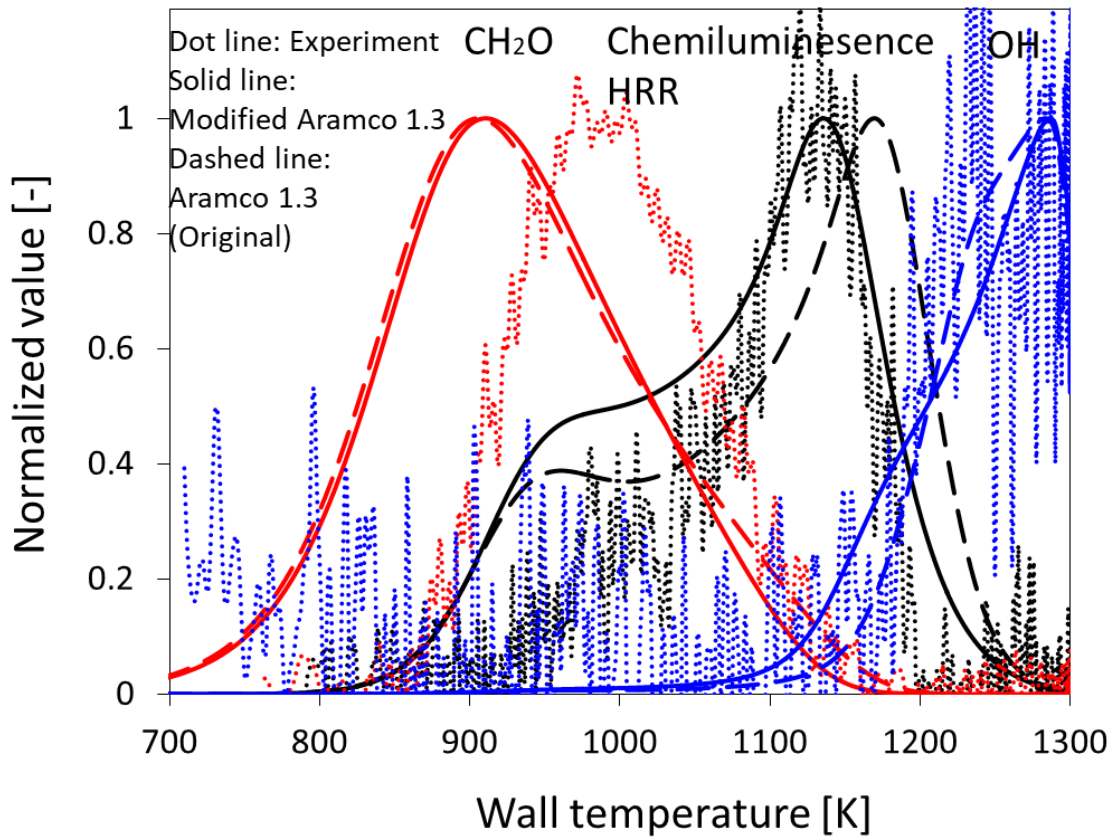
Fig. 19. Normalized intensity of experimentally obtained images and normalized HRR, CH_2O molar

concentration and OH molar concentration computed with the modified mechanism and Aramco 1.3 at

1.0 bar.

Figure 20 depicts the normalized intensity of experimentally obtained images and the normalized HRR, CH_2O molar concentration, and OH molar concentration computed using the modified mechanism and Aramco 1.3 at 5.0 bar. As with results obtained for 1.0 bar, the peak position of the HRR profile computed with the modified mechanism shifts to a lower temperature region than that computed using Aramco 1.3. Results show better agreement with those obtained from the experiment than those computed using Aramco 1.3. However, the present modification does not affect the peak position of the CH_2O profile. The discrepancy in the peak position of the CH_2O profile between experiment and computation remains. This discrepancy is discussed further in Section 4.4. The modified mechanism shows a milder peak of HRR at a lower temperature (*ca.* 900 K) than Aramco 1.3, but the chemiluminescence profile shows no such double peak. This double peak of HRR is discussed in Section 4.5.

Fig. 20. Normalized intensity of experimentally obtained images and normalized HRR, CH_2O molar

concentration and OH molar concentration computed with the modified mechanism and Aramco 1.3 at

5.0 bar.

4.3.13. Validation of the modified mechanism with experimentally obtained results for flame

speeds and ignition delays

Figure 21 shows computational laminar flame speeds obtained using the modified

mechanism and Aramco 1.3, and data from the relevant literature [1–9] for methane/air mixtures

at 1.0, 5.0, and 10.0 bar with initial temperatures of 298–300 K. Laminar flame speeds

computed using the modified mechanism are slightly higher than those computed using Aramco

1.3 (*ca.* 2.5 %), but the modified mechanism satisfactorily predicts experimentally obtained
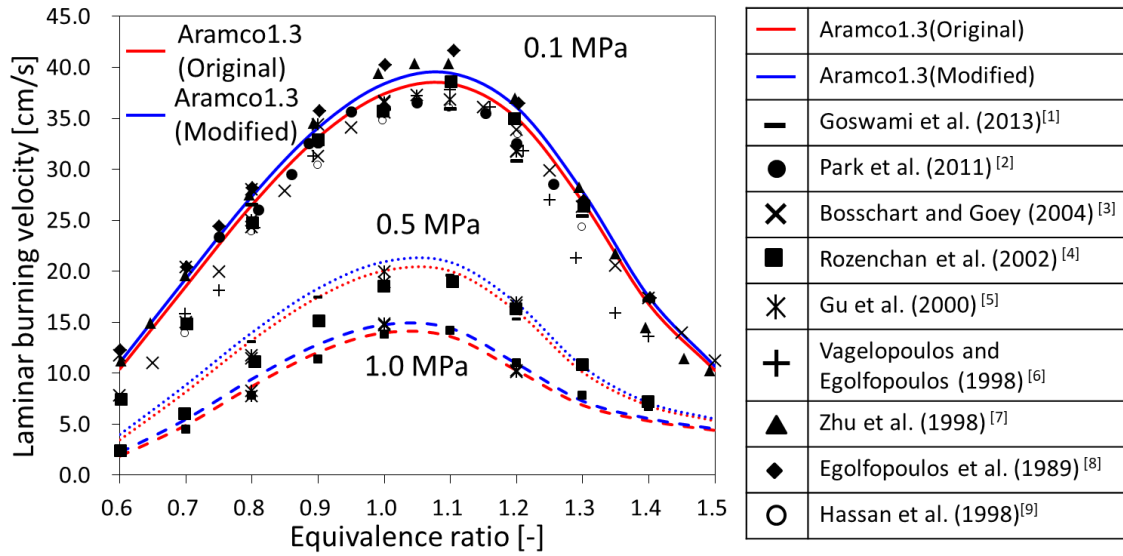
35

laminar flame speeds.

Fig. 21. Computational laminar flame speeds with the modified mechanism and Aramco 1.3 and data in literature [1–9] for methane/air mixtures at 1.0, 5.0, and 10.0 bar and initial temperatures of 298–300 K.

Figure 22 presents computational ignition delay times obtained using the modified mechanism and Aramco 1.3, with experimental data obtained by Burke et al. [14] for methane–air mixtures at 10 and 25 bar and equivalence ratios of 0.3, 0.5, 1.0, and 2.0. The experimentally obtained data of Burke et al. were chosen for validation here because these experiments were lowest temperature and pressure investigated. The modified mechanism predicts slightly shorter ignition delay times than Aramco 1.3 at most conditions, but the predictions using the modified mechanism still show satisfactory agreement with the experimentally obtained results. Moreover, remarkable improvements attributable to the present modification are apparent at "intermediate temperatures" where ignition delay are measured by RCM and the lower pressure of 10 bar.
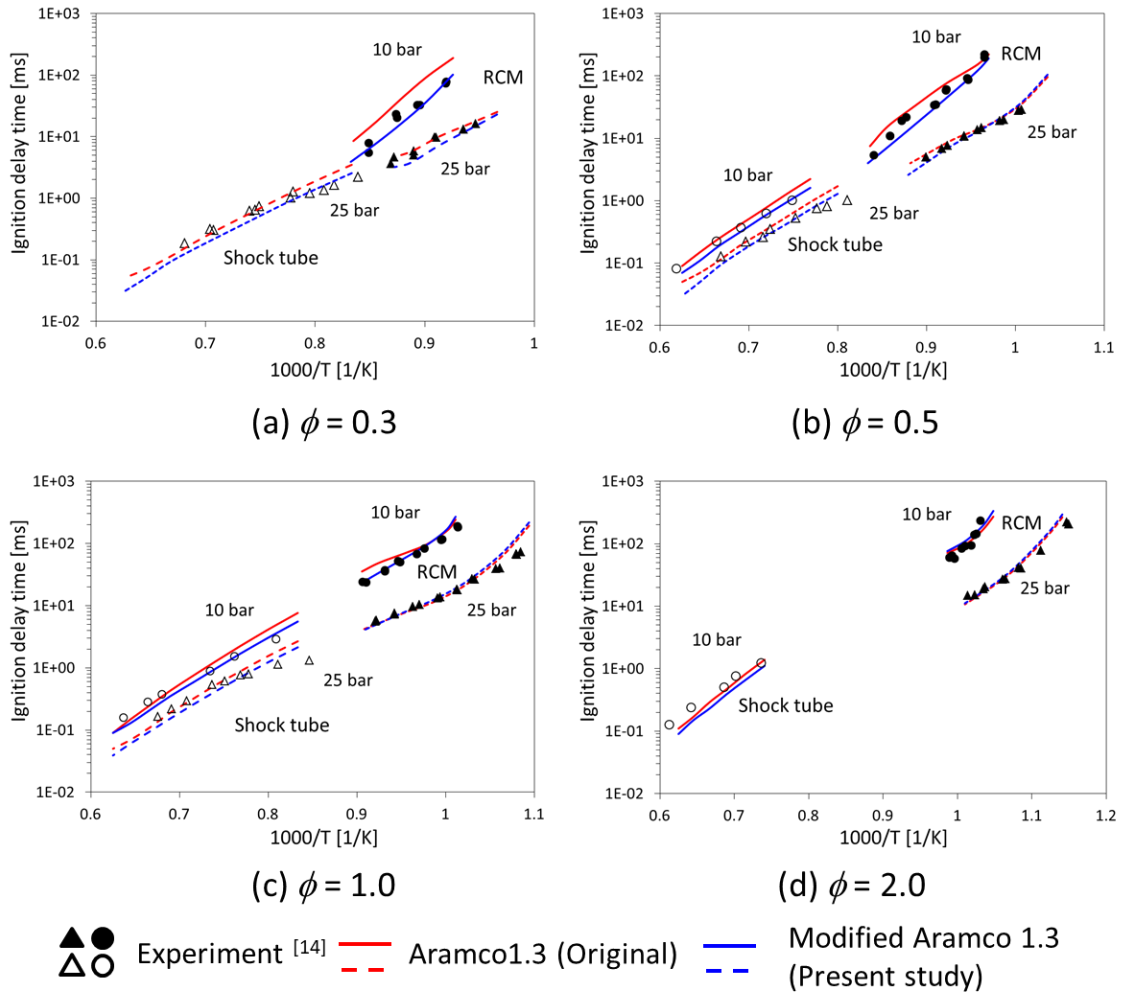
Fig. 22. Computational ignition delay times computed with the modified mechanism and Aramco 1.3 and experimental data obtained by Burke et al. [14] for methane/air mixtures at 10 and 25 bar and equivalence ratios of 0.3, 0.5, 1.0 and 2.0.

4.4. *Intermediate-temperature oxidation chemistry for methane*

The present modification improved predictions for weak flames as well as ignition delays at "*intermediate temperatures*" and low pressures and less affected flame speeds. However, the present modification did not affect the peak position of the CH_2O profile in weak flames at 5.0 bar. The discrepancy between experiments and computations remained. To examine the discrepancy, reaction path analysis was conducted using the modified mechanism.

37

Figure 23 presents reaction pathways of methane weak flames (a) at 1.0 and (b) at 5.0 bar. A large difference in reaction pathways from CH_3 to CH_2O between 1.0 and 5.0 bar is displayed in the figure.

Figure 24 presents results of sensitivity analysis for CH_2O peak position at 5.0 bar: the top 10 reactions. At 5.0 bar condition, R150: $CH_3O_2 + CH_2O \Leftrightarrow CH_3O_2H + HCO$ and R154: $CH_3O_2 + HO_2 \Leftrightarrow CH_3O_2H + O_2$ shows high sensitivity for CH_2O peak position.
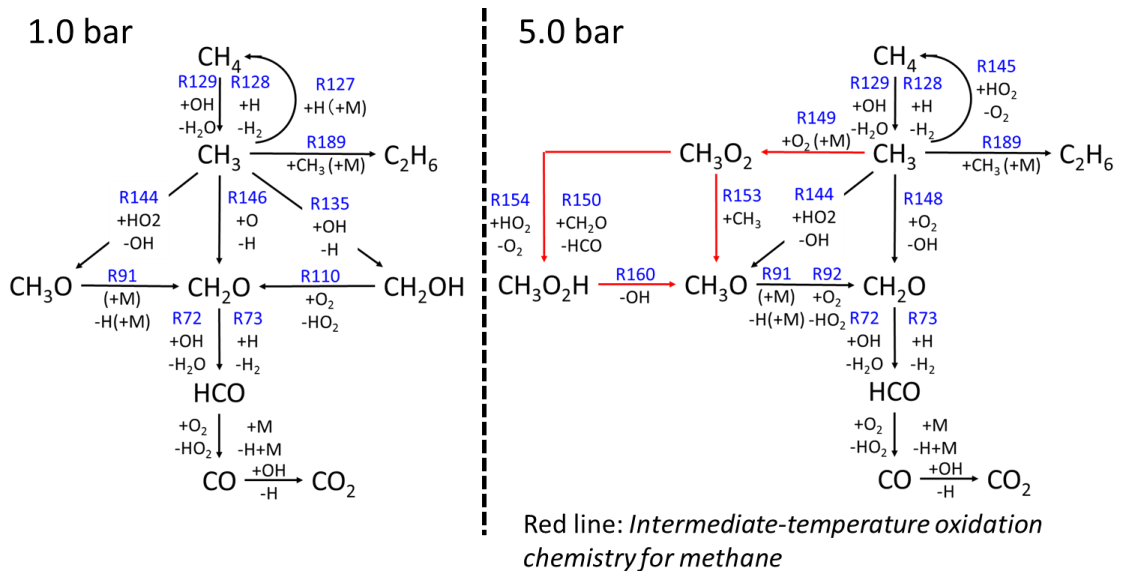
Fig. 23. Main reaction pathways of methane stoichiometric weak flames at 1.0 and 5.0 bar.

Sensitivity coefficient [-]
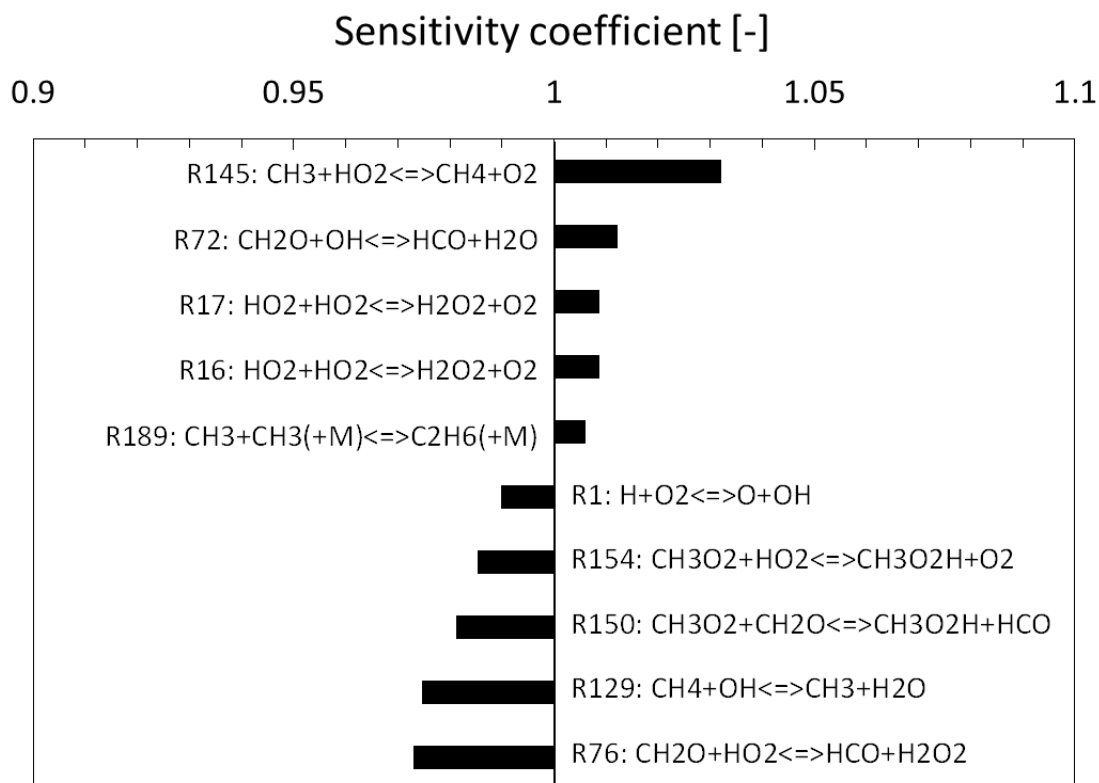
Fig. 24. Sensitivity analysis for CH_2O peak position at 5.0 bar

Three major pathways from CH_3 to CH_2O at 1.0 bar exist: $CH_3 \rightarrow CH_2O$, $CH_3 \rightarrow CH_3O \rightarrow CH_2O$, and $CH_3 \rightarrow CH_2OH \rightarrow CH_2O$. At 5.0 bar, the reaction pathway of $CH_3 \rightarrow CH_2OH \rightarrow CH_2O$ is not a major pathway. The *intermediate-temperature oxidation chemistry for methane*, $CH_3 \rightarrow CH_3O_2 \rightarrow CH_3O_2H \rightarrow CH_3O \rightarrow CH_2O$, and $CH_3 \rightarrow CH_3O_2 \rightarrow CH_3O \rightarrow CH_2O$, becomes important. However, the two reaction paths in the *intermediate-temperature oxidation chemistry for methane* above have not been studied extensively. The only study of rate constants of R154: $CH_3O_2 + HO_2 <=> CH_3O_2H + O_2$ was conducted experimentally by Lightfoot et al. [100]. The temperature conditions in the experiment were 248−700 K. Aramco 1.3 extrapolated these rate constants to higher temperatures. No rate constants of R150: $CH_3O_2 + CH_2O <=> CH_3O_2H + HCO$ have been

39

obtained experimentally or theoretically; the only estimation available is that reported by Tsang

and Hampson [101]. They estimated rate constants of R150 using the analogy with a reaction of

$HO_2 + CH_2O <=> H_2O_2 + HCO$ and also reported large uncertainty. The thermochemical

properties of CH_3O_2 are quite important to calculate the rate of CH_3O_2 production from R149:

$CH_3 + O_2 (+M) <=> CH_3O_2 (+M)$ [102] but a large discrepancy prevails among data reported in

the literature [103–106]. Need for additional study of the *intermediate-temperature oxidation*

chemistry for methane has been indicated [107, 108]. Because experimentally obtained data for

methane ignition characteristics at "intermediate temperatures" are extremely limited because of

the low reactivity of methane, the present CH_2O-LIF results in the micro flow reactor are useful

for mechanism validation, especially for the *intermediate-temperature oxidation chemistry for*

methane.

4.5. Two-stage ignition of methane at high pressure

The modified mechanism showed two peaks in the HRR profile for weak flames at 5.0 bar.

Because the micro flow reactor system suppresses the rapid rise of temperature even in the

reaction zone, it enables the resolution of a single ignition in a transient system as a steady,

multi-stage oxidation in the weak flame regime for large hydrocarbons [18–21]. Earlier studies

also demonstrated that the HRR peak at lower temperature strengthens with increased pressure,

indicating a double peak of the chemiluminescence profile at higher pressures for methane weak

flames. To investigate this point, chemiluminescence observation at 6.0−10.0 bar was conducted.

Chemiluminescence profiles were compared with computational HRR profiles using the

modified mechanism.

Figure 25 presents chemiluminescence images for a stoichiometric methane/air mixture at

40

6.0−10.0 bar. Although chemiluminescence images become noisy because of a lower S/N ratio at higher pressures, the chemiluminescence intensity at temperature around 900−950 K strengthens with increased pressure. Figure 26 depicts a comparison between the normalized chemiluminescence intensity and the normalized HRR at 6.0, 8.0, and 10.0 bar. A distinct peak of the chemiluminescence intensity is apparent at intermediate temperatures of 900−950 K at 6.0 bar. The peak position shows good agreement with the first peak position of the HRR profile. The first chemiluminescence peak becomes stronger with increased pressure; it is almost identical to the second one at 10.0 bar. However, the first HRR peak is stronger than the second one at 8.0 bar in the computations. The comparison reveals that the rate of the increase in the value of the first HRR peak versus pressure is higher than that of the first chemiluminescence peak.

This study has demonstrated the separation of the *intermediate-temperature oxidation chemistry for methane* at elevated pressures, which is a unique characteristic of the present micro flow reactor. However, further improvements of measurements must be undertaken to investigate the chemical kinetics of the *intermediate-temperature oxidation chemistry for methane* through quantitative comparison.
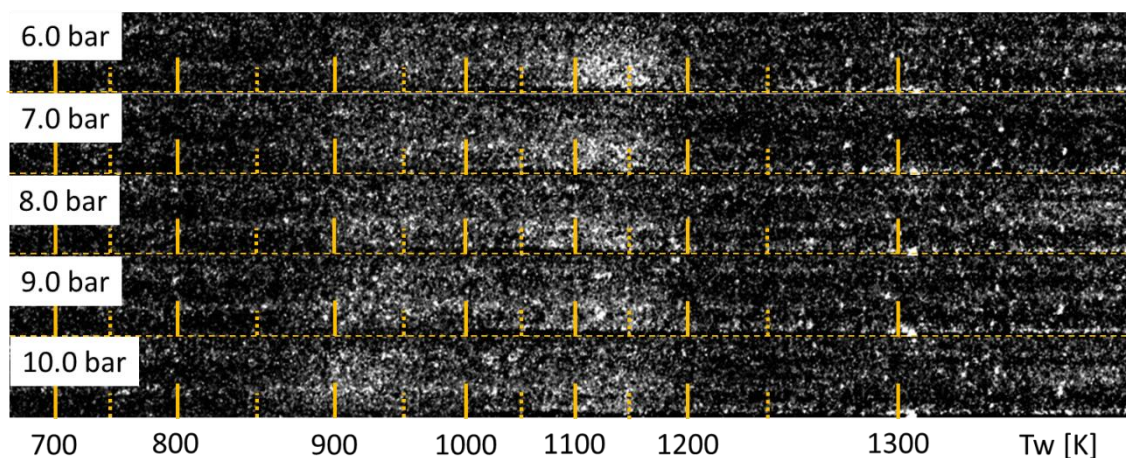
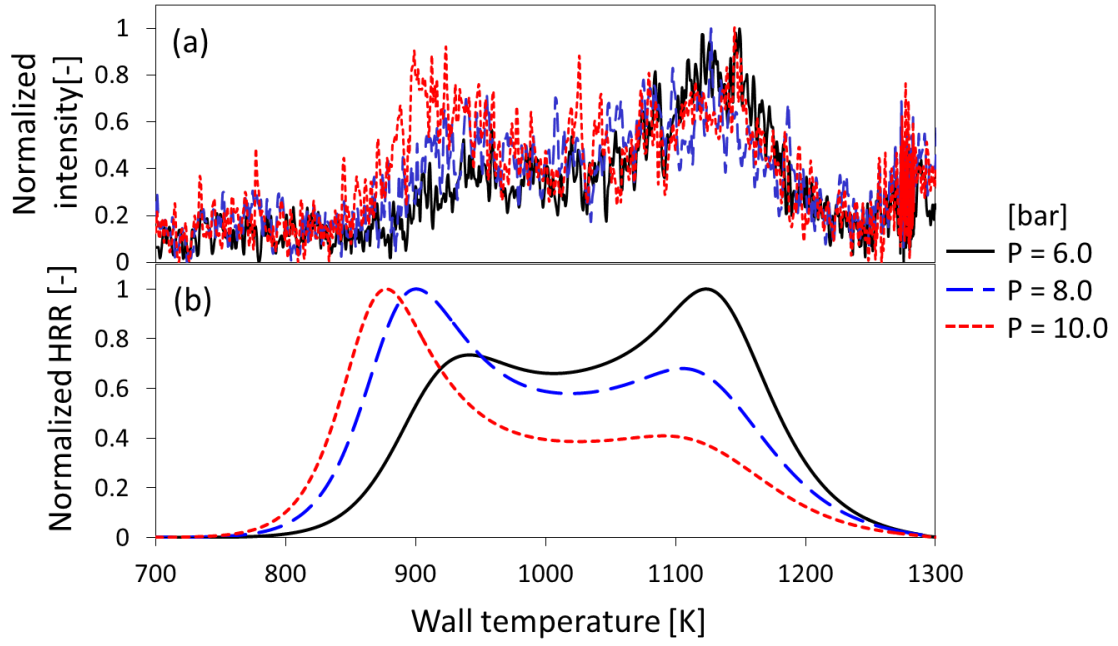Fig. 25. Images of chemiluminescence observation of methane weak flames at 6.0–10.0 bar.

Fig. 26. Luminous intensity of chemiluminescence image and computational HRR profile by the present

modified mechanism at 6.0, 8.0 and 10.0 bar.

5. Conclusions

OH-LIF and CH$_2$O-LIF measurements and chemiluminescence observation were conducted for methane weak flames using a micro flow reactor with a controlled temperature profile at 1.0 and 5.0 bar. Experimental results showed that the luminous regions of CH$_2$O-LIF, chemiluminescence and OH-LIF were located in this order from the upstream side at 1.0 and 5.0 bar. These results demonstrated the capability of LIF-measurements for methane weak flames in the micro flow reactor with a controlled temperature profile (MFR) to observe the spatial separation of CH$_2$O formation in the upstream region of the flame position and the OH formation in the downstream region of the flame position.

One-dimensional computations were conducted with five detailed chemical kinetic models. All mechanisms predicted the CH$_2$O formation in the upstream region of the HRR peak and the OH formation in the downstream region of the HRR peak at both pressures, which is consistent with experimentally obtained results. However, the peak positions in the CH$_2$O, HRR, and OH profiles computed with all the mechanisms showed no quantitative agreement with those in the experimentally obtained profiles.

Modifications of Aramco 1.3 was conducted to reproduce the experimentally obtained results. Through sensitivity analyses for weak flame positions and flame speeds, candidate reactions for modification, which showed high sensitivity for weak flame positions, were chosen. Rate constants of the candidate reactions were adjusted within their uncertainty. The modified mechanism showed better agreement with the experimentally obtained results for weak flames than those of the original mechanism. In addition, the modified mechanism still satisfactorily predicted data reported in the literature for lamina flame speeds and for ignition delay times. Remarkably, the modified mechanism showed better agreement with experimentally obtained ignition delay times at lower temperatures where RCM data is

43

commonly used and lower pressure compared to the original mechanism. This study demonstrated that mechanism validation using weak flame data of MFR is valuable for improving the prediction of ignition delay times at such temperatures and pressures.

Nonetheless, the modified mechanism still predicted the peak position in the CH_2O profile at a lower temperature than experiments. Reason of this discrepancy was examined using reaction path analysis. The results elucidated that the importance to *intermediate-temperature oxidation chemistry for methane* at elevated pressures. The CH_2O-LIF measurements at pressures above 6.0 bar indicated two-stage oxidation of methane. Further studies of methane weak flames in the present micro flow reactor are expected to validate the mechanisms describing the *intermediate-temperature oxidation chemistry for methane*.

References

[1]   M. Goswami, S.C.R. Derks, K. Coumans, W.J. Slikker, M.H. de Andrade Oliveira, R.J.M. Bastiaans, C.C.M. Luijten, L.P.H. de Goey, A.A. Konnov, The effect of elevated pressures on the laminar burning velocity of methane + air mixtures, Combust. Flame 160 (2013) 1627–1635.

[2]   O. Park, P.S. Veloo, N. Liu, F. N. Egolfopoulos, Combustion characteristics of alternative gaseous fuels, Proceedings of the Combustion Institute 33 (2011) 887–894.

[3]   K.J. Bosschaart, L.P.H. de Goey, The laminar burning velocity of flames propagating in mixtures of hydrocarbons and air measured bywith the heat flux method, Combust. Flame 136 (2004) 261–269.

[4]   G. Rozenchan, D.L. Zhu, C.K. Law, S.D. Tse, Outward propagation, burning velocities, and chemical effects of methane flames up to 60 ATM, Proceedings of the Combustion Institute 29 (2002) 1461–1469.

[5]   X.J. Gu, M.Z. Haq, M. Lawes, R. Woolley, Laminar burning velocity and Markstein lengths of methane–air mixtures, Combust. Flame 121 (2000) 41–58.

[6]   C.M. Vagelopoulos, F.N. Egolfopoulos, Direct experimental determination of laminar flame speeds, Proceedings of the Combustion Institute 27 (1998) 513–519.

[7]   D.L. Zhu, F.N. Egolfopoulos, C.K. Law, Experimental and numerical determination of laminar flame speeds of methane/(Ar, N_2, CO_2)-air mixtures as function of stoichiometry, pressure, and flame temperature, Proceedings of the Combustion Institute 22 (1988) 1537–1545.

[8]   F.N. Egolfopoulos, P. Cho, C.K. Law, Laminar flame speeds of methane-air mixtures under reduced and elevated pressures, Combust. Flame 76 (1989) 375–391.

[9]   M.I. Hassan, K.T. Aung, G.M. Faeth, Measured and predicted properties of laminar

premixed methane/air flames at various pressures, Combust. Flame 115 (1998) 539–550.

[10]   C.J. Aul, W.K. Metcalfe, S.M. Burke, H.J. Curran, E.L. Petersen, Ignition and kinetic modeling of methane and ethane fuel blends with oxygen: A design of experiments approach, Combust. Flame 160 (2013) 1153–1167.

[11]   J. Huang, P.G. Hill, W.K. Bushe, S.R. Munshi, Shock-tube study of methane ignition under engine-relevant conditions: experiments and modeling, Combust. Flame 136 (2004) 25–42.

[12]   E. Hu, X. Li, X. Meng, Y. Che, Y. Xie, Z. Huang, Laminar flame speeds and ignition delay times of methane–air mixtures at elevated temperatures and pressures, Fuel 158 (2015) 1–10.

[13]   J. de Vries, E.L. Petersen, Autoignition of methane-based fuel blends under gas turbine conditions, Proc. Combust. Inst. 31 (2007) 3163–3171.

[14]   U. Burke, K.P. Somers, P. O'Toole, C.M. Zinner, N. Marquet, G. Bourque, E.L. Petersen, W.K. Metcalfe, Z. Serinyel, H.J. Curran, An ignition delay and kinetic modeling study of methane, dimethyl ether, and their mixtures at high pressures, Combust. Flame 162 (2015) 315–330.

[15]   R. Zhu, M.C. Lin, The CH_3 + HO_2 Reaction: First-Principles Prediction of its Rate Constant and Product Branching Probabilities, J. Phys. Chem. A 105 (2001) 6243–6248.

[16]   K. Maruta, T. Kataoka, N.I. Kim, S. Minaev, R. Fursenko, Characteristics of combustion in a narrow channel with a temperature gradient, Proc Combust. Inst. 30(2) (2005) 2429–2436.

[17]   H. Oshibe, H. Nakamura, T. Tezuka, S. Hasegawa, K. Maruta, Stabilized three-stage

46

oxidation of DME/air mixture in a micro flow reactor with a controlled temperature profile, Combust. Flame 157 (2010) 1572–1580.

[18]   A. Yamamoto, H. Oshibe, H. Nakamura, T. Tezuka, S. Hasegawa, K. Maruta, Stabilized three-stage oxidation of gaseous n-heptane/air mixture in a micro flow reactor with a controlled temperature profile, Proc. Combust. Inst. 33 (2011) 3259–3266.

[19]   S. Suzuki, M. Hori, H. Nakamura, T. Tezuka, S. Hasegawa, K. Maruta, Study on cetane number dependence of diesel surrogates/air weak flames in a micro flow reactor with a controlled temperature profile, Proc. Combust. Inst. 34(2) (2013) 3411–3417.

[20]   M. Hori, A. Yamamoto, H. Nakamura, T. Tezuka, S. Hasegawa, K. Maruta, Study on octane number dependence of PRF/air weak flames at 1–5 atm in a micro flow reactor with a controlled temperature profile, Combust. Flame 159 (2012) 959–967.

[21]   M. Hori, H. Nakamura, T. Tezuka, S. Hasegawa, K. Maruta, Characteristics of n-heptane and toluene weak flames in a micro flow reactor with a controlled temperature profile, Proc. Combust. Inst. 34 (2013) 3419–3426.

[22]   T. Kamada, H. Nakamura, T. Tezuka, S. Hasegawa, K. Maruta, Study on combustion and ignition characteristics of natural gas components in a micro flow reactor with a controlled temperature profile, Combust. Flame 161 (2014) 37–48.

[23]   H. Nakamura, H. Takahashi, T. Tezuka, S. Hasegawa, K. Maruta, K. Abe, Effects of CO-to-H_2 ratio and diluents on ignition properties of syngas examined by weak flames in a micro flow reactor with a controlled temperature profile, Combust. Flame 172 (2016) 94–104.

[24]   S. Kikui, H. Nakamura, T. Tezuka, S. Hasegawa, K. Maruta, Study on combustion and

ignition characteristics of ethylene, propylene, 1-butene and 1-pentene in a micro flow

reactor with a controlled temperature profile, Combust. Flame 163(1) (2016) 209–219.

[25]   H. Nakamura, S. Hasegawa Combustion and ignition characteristics of ammonia/air

mixtures in a micro flow reactor with a controlled temperature profile, Proc. Combust.

Inst. 36 (2017) 4217–4226.

[26]   H. Nakamura, S. Hasegawa, T. Tezuka, Kinetic modeling of ammonia/air weak flames

in a micro flow reactor with a controlled temperature profile, Combust. Flame 185

(2017) 16–17.

[27]   T. Shimizu, H, Nakamura, T. Tezuka, S. Hasegawa, K. Maruta, OH and CH_2O

Laser-Induced Fluorescence Measurements for Hydrogen Flames and Methane,

n-Butane, and Dimethyl Ether Weak Flames in a Micro Flow Reactor with a

Controlled Temperature Profile, In press.

[28]   Y. Tuboi, T. Yokomori, K. Maruta, Lower limit of weak flame in a heated channel,

Proc. Combust. Inst. 32(2) (2009) 3075–3081.

[29]   K. Kohse-Höinghaus, J.B. Jefferies, J.B. Applied Combustion Diagnostics; Taylor &

Francis Group: New York, 2002.

[30]   H. Kobayashi, Experimental study of high-pressure turbulent premixed flames. Exp.

Therm. Fluid Sci. 26 (2002) 375−387.

[31]   K. Yamamoto, M. Ozeki, N. Hayashi, H. Yamashita, Burning velocity and OH

concentration in premixed combustion, Proc. Combust. Inst. 32 (2009) 1227−1235.

[32]   C. Brackmann, J. Nygren, X. Bai, Z. Li, H. Bladh, B. Axelsson, I. Denbratt, L.

Koopmans, P.E. Bengtsson, M. Aldén, Laserinduced fluorescence of formaldehyde in

combustion using third harmonic Nd:YAG laser excitation, Spectrochim. Acta, Part A

59 (2003) 3347−3356.

48

[33] H. Haessler, H. Bockhorn, C. Pfeifer, D. Kuhn, Formaldehyde-LIF of dimethyl ether during auto-ignition at elevated pressures, Flow, Turbul. Combust. 89 (2012) 249−259.

[34] D.C. Kyritsis, V.S. Santoro, A. Gomez, The effect of temperature correction on the measured thickness of formaldehyde zones in diffusion flames for 355 nm excitation, Experiments in Fluids 37 (2004) 769–772.

[35] Y. Tuboi, T. Yokomori, K. Maruta, Lower limit of weak flame in a heated channel, Proc. Combust. Inst. 32 (2009) 3075–3081.

[36] K. Maruta, T. Kataoka, N. I. Kim, S. Minaev, R. Fursenko, Characteristics of combustion in a narrow channel with a temperature gradient, Proc Combust. Inst. 30(2) (2005) 2429–2436.

[37] G.P. Smith, D.M. Golden, M. Frenklach, N.W. Moriarty, B. Eiteneer, M.Goldenberg, C.T. Bowman, R.K. Hanson, S. Song, W.C. Gardiner, Jr., V.V. Lissianski, Z. Qin, available at http://www.me.berkeley.edu/gri_mech/

[38] The San Diego Mechanism, version2014_10_04, available at http://web.eng.ucsd.edu/mae/groups/combustion/mechanism.

[39] USC Mech Version II, available at http://ignis.usc.edu/Mechanisms/USC-Mech%20II/USC_Mec h%20II.htm

[40] W.K. Metcalfe, S.M. Burke, S.S. Ahmed, H.J. Curran, A Hierarchical and Comparative Kinetic Modeling Study of $C_1−C_2$ Hydrocarbon and Oxygenated Fuels, Int. J. Chem. Kinet. 45(10) (2003) 638–675.

[41] HP-mech 3.3, http://engine.princeton.edu/mechanism/HP-Mech.html

[42] S. Kikui, H. Nakamura, T. Tezuka, S. Hasegawa, K. Maruta, Characteristics of n-butane weak flame at elevated pressures in a micro flow reactor with a controlled

49

temperature profiles, Proc. Combust. Inst. 35 (3) (2015) 3405–3412.

[43]   T. Okuno, H. Nakamura, T. Tezuka, S. Hasegawa, K. Maruta, Ultra-lean combustion
       characteristics of premixed methane flames in a micro flow reactor with a controlled
       temperature profile, Proc. Combust. Inst. 36(3) (2017) 4227–4233.

[44]   Z. Hong, D.F. Davidson, K.-Y. Lam, R.K. Hanson, A shock tube study of the rate
       constants of HO_2 and CH_3 reactions, Combust. Flame 159 (2012) 3007–3013.

[45]   J.J. Scire Jr., F.L. Dryer, R.A. Yetter, Comparison of global and local sensitivity
       techniques for rate constants determined using complex reaction mechanisms, Int. J.
       Chem. Kinet. 33 (2001) 784–802.

[46]   T.V.-T. Mai, M. v. Duong, X.T. Le, L.K. Huynh, A. Ratkiewicz, Direct ab initio
       dynamics calculations of thermal rate constants for the $CH_4 + O_2 = CH_3 + HO_2$
       reaction, Struct. Chem. 25 (2014) 1495–1503.

[47]   A.W. Jasper, S.J. Klippenstein, L.B. Harding, Theoretical rate coefficients for the
       reaction of methyl radical with hydroperoxyl radical and for methylhydroperoxide
       decomposition, Proc. Combust. Inst. 32 (2009) 279–286.

[48]   C. Yan, L.N. Krasnoperov, Reaction of CH_3 Radicals with HO_2, International
       Conference on Chemical Kinetics 2015, Ghent, Belgium, Lecture O21.

[49]   E.P. Faragó, M. Szöri, C. Owen, B. Viskolcz, Critical evaluation of the potential
       energy surface of the $CH_3 + HO_2$ reaction system, J. Chem. Phys. 142(5) (2015)
       054308.

[50]   M. Sangwan, C. Yan, E.N. Chesnokov, L.N. Krasnoperov, Kinetics of the Gas Phase
       Reaction $CH_3 + HO_2$, J Phys. Chem. A 119 (2015) 7848–7857.

[51]   B. Wang, H. Hou, L.M. Yoder, J.T. Muckerman, C. Fockenberg, Experimental and
       Theoretical Investigations on the Methyl–Methyl Recombination Reaction, J. Phys.

50

Chem. A 107 (2003) 11414–11426.

[52]   I.R. Slagle, D. Gutman, J.W. Davis, M.J. Pilling, Study of the Recombination Reaction

$CH_3 + CH_3 \rightarrow C_2H_6$. 1. Experiment, J. Phys. Chem. 92 (1988) 2455–2462.

[53]   S.J. Klippenstein, Y. Georgievskii, L.B. Harding, Predictive theory for the

combination kinetics of two alkyl radicals, Phys. Chem. Chem. Phys. 8 (2006) 1133–

1147.

[54]   S.J. Klippenstein, L.B. Harding, A Direct Transition State Theory Based Study of

Methyl Radical Recombination Kinetics, J. Phys. Chem. A 103 (1999) 9388–9398.

[55]   A.F. Wagner, D.M. Wardlaw, Study of the Recombination Reaction $CH_3 + CH_3 \rightarrow$

C_2H_6. 2. Theory, J. Phys. Chem. 92 (1988) 2462–2471.

[56]   C.J. Cobos, J. Troe, Theory of thermal unimolecular reactions at high pressures. II.

Analysis of experimental results, J. Chem. Phys. 83(3) (1985) 1010–1015.

[57]   G. Hancock, V. Haverd, M. Morrison, Infrared emission accompanying the gas phase

recombination of alkyl radicals, Phys. Chem. Chem. Phys. 5 (2003) 2981–2987.

[58]   H. Du, J.P. Hessler, P.J. Ogren, Recombination of Methyl Radicals. 1. New Data

between 1175 and 1750 K in the Falloff Region, J. Phys. Chem. 100 (1996) 974–983.

[59]   H. Hippler, K. Luther, A.R. Ravishankara, J. Troe, High-Pressure Effects in the

Recombination Reaction $CH_3 + CH_3 \rightarrow C_2H_6$, Z. Phys. Chem. Neue. Fol. 142 (1984)

1–12.

[60]   M.T. Macpherson, M.J. Pilling, M.J. Smith, J Determination of the Absorption Cross

Section for CH_3, at 216.36 nm and the Absolute Rate Constant for Methyl Radical

Recombination over the Temperature Range 296–577 K, J. Phys. Chem. 89 (1985)

2268–2274.

[61]   K. Glänzer, M. Quack, J. Troe, A Spectroscopic Determination of the Methyl Radical

51

Recommendation Rate constant in Shock Waves, Chem. Phys. Lett. 39 (1976) 304–309.

[62]   D.L. Baulch, C.T. Bowman, C.J. Cobos, R.A. Cox, Th. Just, J.A. Kerr M.J. Pilling, D. Stocher, J. Troe, W. Tsang, R.W. Walker, J. Warnatz, Evaluated Kinetic Data for Combustion Modeling: Supplement II, J. Phys. Chem. Ref. Data 34(3) (2005) 757–1397.

[63]   N.K. Srinivasan, M.-C. Su, J.W. Sutherland, J.V. Michael, Reflected Shock Tube Studies of High-Temperature Rate Constants for $OH + CH_4 \rightarrow CH_3 + H_2O$ and $CH_3 + NO_2 \rightarrow CH_3O + NO$, J. Phys. Chem. A 109 (2005) 1857–1863.

[64]   M.G. Bryukov, V.D. Knyazev, S.M. Lomnicki, C.A. McFerrin, B. Dellinger, Temperature-Dependent Kinetics of the Gas-Phase Reactions of OH with Cl_2, CH_4, and C_3H_8, J. Phys. Chem. A 108 (2004) 10464–10472.

[65]   A. Bonard, V. Daële, J.-L. Delfau, C. Vovelle, Kinetics of OH Radical Reactions with Methane in the Temperature Range 295–660 K and with Dimethyl Ether and Methyl-tert-butyl Ether in the Temperature Range 295–618 K, J. Phys. Chem. A 106 (2002) 4384–4389.

[66]   J.R. Dunlop, F.P. Tully, A Kinetic Study of OH Radical Reactions with Methane and Perdeuterated Methane, J. Phys. Chem. 97 (1993) 11148–11150.

[67]   S. Madronich, W. Felder, Direct Measurements of the Rate Coefficient for the Reaction $OH + CH_4 \rightarrow CH_3 + H_2O$ Over 300–1500 K, Symp. (Int.) Combust. 20(1) 1985 703–713.

[68]   L. Masgrau, À. González-Lafont, J.M. Lluch, The reactions $CHn\ D_{4-n} + OH \rightarrow P$ and $CH_4 + OD \rightarrow CH_3 + HOD$ as a test of current direct dynamics multicoefficient methods to determine variational transition state rate constants. II, J. Chem. Phys. 115 (2001)

4515–4526.

[69]   M. Schwartz, P. Marshall, R.J. Berry, C.J. Ehlers, G.A. Petersson, Computational Study of the Kinetics of Hydrogen Abstraction from Fluoromethanes by the Hydroxyl Radical, J. Phys. Chem. A 102 (1998) 10074–10081.

[70]   J.W. Sutherland, M.-C. Su, J.V. Michael, Rate constants for H+CH$_4$, CH$_3$+H$_2$, and CH$_4$ dissociation at high temperature, Int. J. Chem. Kinet. 33 (2001) 669–684.

[71]   M.G. Bryukov, I.R. Slagle, V.D. Knyazev, Kinetics of reactions of H atoms with methane and chlorinated methanes, J. Phys. Chem. A 105 (2001) 3107–3122.

[72]   H.J. Baeck, K.S. Shin, H. Yang, Z. Qin, V. Lisslanski, W.C. Gardinaer, Jr., Shock tube study of the reaction between CH$_3$ and H$_2$, J. Phys. Chem. 99 (1995) 15925–15929.

[73]   M.J. Rabinowitz, J.W. Sutherland, P.M. Patterson, R.B. Klemm, Direct rate constants measurements for H+CH$_4$→CH$_3$+H$_2$, 897–1729 K, using the flash photolysis–shock tube technique, J. Phys. Chem. 95 (1991) 674–681.

[74]   B. Kerkeni, D.C. Clary, Kinetics isotope in the reactions of D atoms with CH$_4$, C$_2$H$_6$, and CH$_3$OH: quantum dynamics calculations, J. Phys. Chem. A 108 (2004) 8966–8972.

[75]   V. Vasudevan, D.F. Davidson, R.K. Hanson, Direct Measurements of the Reaction OH + CH$_2$O → HCO + H$_2$O at High Temperatures, Int. J. Chem. Kinet. 37 (2005) 98–109.

[76]   V. Sivakumaran, D. Hölscher, T.J. Dillon, J.N. Crowley, Reaction between OH and HCHO: temperature dependent rate coefficients (202–399 K) and product pathways (298 K), Phys. Chem. Chem. Phys. 5 (2003) 4821–4827.

[77]   J.F. Bott, N. Cohen, A shock tube study of the reactions of the hydroxyl radical with several combustion species, Int. J. Chem. Kinet. 23 (1991) 1075–1094.

[78]   S. Zabarnick, J.W. Fleming, M.C. Lin, Kinetics of hydroxyl radical reactions with

formaldehyde and 1,3,5-trioxane between 290 and 600 K, Int. J. Chem. Kinet. 20 (1988) 117–129.

[79]   L.O. de Gurtechin, J. Vandooren, P.J. Van Tiggelen, Radical reactions in formaldehyde flames, Bull. Soc. Chim. Belg. 92 (1983) 663–664.

[80]   R. Atkinson, J.N. Pitts, Jr., Kinetics of the reactions of the OH radical with HCHO and CH_3CHO over the temperature range 299–426K, J. Chem. Phys. 68 (1978) 3581–3584.

[81]   J. Peeters, G. Mahnen, Reaction Mechanisms and Rate Constants of Elementary Steps in Methane–Oxygen Flames, Symp. (Int.) Combust. 14 (1973) 133–146.

[82]   A.A. Westenberg, R.M. Fristrom, H and O atom profiles measured by ESR in C_2 hydrocarbon-O_2 flames, Symp. (Int.) Combust. 10 (1965) 473–487.

[83]   S. Xu, R.S. Zhu, M.C. Lin, Ab Initio Study of the OH+CH_2O Reaction: The Effect of the OH··OCH_2 Complex on the H-Abstraction Kinetics, Int. J. Chem. Kinet. 38 (2006) 322–326.

[84]   H.Y. Li, M. Pu, Y.Q. Ji, Z.-F. Xu, W.L. Feng, Theoretical study on the reaction path and rate constants of the hydrogen atom abstraction reaction of CH_2O with CH_3/OH, Chem. Phys. 307 (2004) 35–43.

[85]   B. Eiteneer, C.L. Yu, M. Goldenberg, M. Frenklach, Determination of Rate Coefficients for Reactions of Formaldehyde Pyrolysis and Oxidation in the Gas Phase, J. Phys. Chem. A 102 (1998) 5196–5205.

[86]   Y. Hidaka, T. Taniguchi, T. Kamesawa, H. Masaoka, K. Inami, H. Kawano, High temperature pyrolysis of formaldehyde in shock waves, Int. J. Chem. Kinet. 25 (1993) 305–322.

[87]   A.A. Jemi-Alade, P.D. Lightfoot, R. Lesclaux, A flash photolysis study of the HO_2 +

HCHO--+H_2O_2 + HCO reaction between 541 and 656 K, Chem. Phys. Lett. 198(1) (1992) 25–30.

[88] S. Hochgreb, F.L. Dryer, A Comprehensive Study on CH_2O Oxidation Kinetics, Combust. Flame 91 (1992) 257–284.

[89] R.R. Baldwin, R.W. Walker, Rate Constants for Reactions of HO_2 Radicals with Alkens, Aldehydes and Related Compounds, Symp. (Int.) Combust. 17(1) (1979) 525–533.

[90] Q.S. Li, X. Zhang, S.W. Zhang, Direct Dynamics Study on the Hydrogen Abstraction Reaction CH_2O + HO_2 → CHO + H_2O_2, J. Phys. Chem. A 109 (2005) 12027–12035.

[91] R.R. Baldwin, P.N. Jones, R.W. Walker, Determination of the rate constant for HO_2+ CH_4→ H_2O_2+ CH_3 at 443°C, J. Chem. Soc. Faraday Trans. 2 84 (1988) 199–207.

[92] H.-H. Carstensen, A.M. Dean, O. Deutschmann, Rate constants for the H abstraction from alkanes (R–H) by R'O_2 radicals: A systematic study on the impact of R and R', Proc. Combust. Inst. 31 (2007) 149–157.

[93] J. Aguilera-Iparraguirre, H.J. Curran, W. Klopper, J.M. Simmie, Accurate Benchmark Calculation of the Reaction Barrier Height for Hydrogen Abstraction by the Hydroperoxyl Radical from Methane. Implications for C_nH_{2n+2} where n = 2 → 4, J. Phys. Chem. A 112 (2008) 7047–7054.

[94] N.K. Srinivasan, M.-C. Su, J.V. Michael, CH_3 + O_2 → H_2CO + OH Revisited, J. Phys. Chem. 111 (2007) 11589–11591.

[95] N.K. Srinivasan, M.-C. Su, J.W. Sutherland, J.V. Michael, Reflected Shock Tube Studies of High-Temperature Rate Constants for CH_3 + O_2, H_2CO + O_2, and OH + O_2, J. Phys. Chem. A 109 (2005) 7902–7914.

[96] C.-L. Yu, C. Wang, M. Frenklach, Chemical Kinetics of Methyl Oxidation by

Molecular Oxygen, J. Phys. Chem. 99 (1995) 14377–14387.

[97]   R. Zhu, C.-C. Hsu, M.C. Lin, Ab initio study of the $CH_3 + O_2$ reaction: Kinetics, mechanism and product branching Probabilities, J. Chem. Phys. 115 (2001) 195–203.

[98]   R. Zellner, F. Ewig, Computational Study of the $CH_3 + O_2$ Chain Branching Reaction, J. Phys. Chem. 92 (1988) 2971–2974.

[99]   M.A. Reitel'boim, L.B. Romanovich, B.I. Vedeneev, Calculation, Based on RRKM Theory of Certain Channels of Interaction of Methyl Radical with Oxygen, Kinet. Catal. 19 (1978) 1131–1136.

[100]   P.D. Lightfoot, P. Roussel, F. Caralp, R. Lesclaux, Flash photolysis study of the CH_3O_2 + CH_3O_2 and CH_3O_2 + HO_2 reactions between 600 and 719 K: unimolecular decomposition of methylhydroperoxide, J. Chem. Soc. Faraday Trans. 87 (1991) 3213–3220.

[101]   W. Tsang, R.F. Hampson, Chemical kinetic Base for Combustion Chemistry. Part 1. Methane and Related Compounds, J. Phys. Chem. Ref. Data 15 (1986) 1087–1222.

[102]   J. Bugler, K.P. Somers, E.J. Silke, H.J. Curran, Revisiting the kinetics and thermodynamics of low-temperature oxidation pathways of alkanes: A case study of the three pentane isomers, J. Phys. Chem. A 119(28) (2015) 7510–7527.

[103]   H. Hashemi, J.M. Christemsen, S. Gersen, H. Levinsky, S.J. Klippenstein, P. Glarborg, High-pressure oxidation of methane, Combust. Flame 172 (2016) 349–364.

[104]   A. Burcat, Burcat's thermodynamic data. Laboratory for Chemical Kinetics. Available at http://garfield.chem.elte.hu/Burcat/burcat.html

[105]   H. Wang, J.W. Bozzelli, Thermochemical Properties (ΔfH°(298 K), S°(298 K), Cp(T)) and Bond Dissociation Energies for C_1−C_4 Normal Hydroperoxides and Peroxy Radicals, J. Chem. Eng. Data 61 (2016) 1836–1849.

[106]   C.F. Goldsmith, G.R. Magoon, W.H. Green, Database of Small Molecule Thermochemistry for Combustion, J. Phys. Chem. A 116 (2012) 9033–9057.

[107]   E.L. Petersen, D.F. Davidson, R.K. Hanson, Kinetics modeling of shock-induced ignition in low-dilution CH_4/O_2 mixtures at high pressures and intermediate temperatures, Combust. Flame 117 (1999) 272–290.

[108]   J.K. Lefkowitz, P. Guo, A. Rousso, Y. Ju, Low temperature oxidation of methane in a nanosecond pulsed plasma discharge, 53rd AIAA Aerospace Sciences Meeting, Kissimmee, FL, 5–9 January. American Institute of Aeronautics and Astronautics. AIAA SciTech Forum, (AIAA 2015–0665).